

Effective synchronization amid noise-induced chaos

Benjamin Sorkin*

Princeton Center for Theoretical Science, Princeton University, Princeton 08544, New Jersey, USA

Thomas A. Witten†

Department of Physics and James Franck Institute, The University of Chicago, Chicago 60637, Illinois, USA

Two remote agents with synchronized clocks may use them to act in concert and communicate. This necessitates some means of creating and maintaining synchrony. One method, not requiring any direct interaction between the agents, is exposing them to a common, environmental, stochastic forcing. This “noise-induced synchronization” only occurs under sufficiently mild forcing; stronger forcing disrupts synchronization. We investigate the regime of strong noise, where the clocks’ phases evolve chaotically. Using a simple realization of disruptive noise, we demonstrate effective synchronization. Namely, although the phases of the two clocks vary erratically, their probability distributions at a given moment become identical. We exploit this statistical synchrony to define an effective phase for an agent that closely agrees with the other’s phase. We discuss how this synchronization of ensembles broadens the range in which noise-induced synchronization can be used, and how it might be exploited in living systems.

SIGNIFICANCE STATEMENT

In ecology and neurobiology, independent living agents may anticipate one another’s behavior by means of a shared measure of time, e.g. simple chemical clocks requiring constant synchronization. We consider the effect of random events in the agents’ common environment that disrupt synchronization. We show that despite the resultant chaotic dynamics of their clocks, the two agents can independently analyze the recent history of the environmental noise to recover effective synchronization. This scheme offers a route to explain how coordinated behavior can emerge amid shared disruptive noise. An example is the puzzling large information transfer encoded in spike timings of sensory neurons.

I. INTRODUCTION

Living systems and man-made machines often depend on the cooperation amongst independent agents. This cooperation is often attained using chemical [1–3], electrical [4–7], or mechanical [8] periodic processes (“clocks”), operating in each agent. Agents with synchronized clocks can exhibit emergent collective phenomena and are able to communicate [9–12]. Since independent clocks inevitably lose synchronization over time, some means are needed in order to achieve and maintain synchronization.

One such means is noise-induced synchronization, occurring when identical noninteracting oscillators are subjected to a common stochastic perturbation from their environment [10, 13–21]. It is distinct from synchronization due to interactions between the clocks and from phase locking unto an external clock. Instead, synchronization is enabled via the clocks’ shared ambient noise. As such, noise-induced synchronization is the only means of maintaining synchroniza-

tion between noninteracting clocks in a generic environment. When the noise is sufficiently mild, it can bring and keep the two oscillators in synchrony over time. This has been well characterized experimentally in a range of physical contexts, such as electric circuits [18], quantum optics signaling [22], and even gene regulatory networks [23]. Synchronization can enable time-based communication between a sender and a receiver. If the sender emits an impulse when its clock is at a particular phase, the receiver can infer this phase by noting its own clock’s phase at the moment of the impulse.

There is no guarantee that two oscillators will synchronize under a given noise. In general, synchronization requires the strength of the noise to lie below a threshold. Beyond this threshold, the relative phase of the two oscillators devolves into chaos [15, 21]. In the latter case, synchronization is lost and with it the means of time-based communication outlined above. Nevertheless, we show below that a form of synchronization persists in the statistical properties of these erratically evolving phases. It permits each agent to define an effective phase that agrees with that of other agents to a quantitatively predictable extent, thus enabling effective synchronization.

We demonstrate this behavior using a simplified type of noise, consisting of randomly timed impulses. For example, this may represent an electric shock applied to a collection of firing neurons [4, 6, 7] or a chemical affecting the cell cycle added into a cell culture [3], at stochastic times. We study the effect of these perturbations on a distribution of phases. Successive impulses create a sequence of phase distributions that in general depend on the initial distribution and the timings of the impulses. In below-threshold noise-induced synchronization, these distributions become narrow and unimodal, concentrated at a single phase. For noises above the threshold, the distributions remain spread over the entire phase circle [21].

The above-threshold effective synchronization we report here arises by virtue of two properties: First, though the distributions change markedly with each impulse, we find that they become independent of the initial state. This means that two initially different oscillator ensembles become statistically identical when compared at a given instant. Second, the distributions can be tightly bunched into a few sharp peaks.

* bs4171@princeton.edu

† t-witten@uchicago.edu

Indeed, when the threshold of synchronization is approached from above, the distributions show a high degree of order, since their average entropy becomes arbitrarily negative [21].

To demonstrate this effect, we follow two different initial phase distributions for two agents A and B. We numerically determine their phase distributions $q_A^{(k)}(\varphi)$ and $q_B^{(k)}(\varphi)$ achieved after a sequence of k impulses (“kicks”), which progressively converge with more kicks into a single distribution determined by the recent history of random waiting times. We propose an effective phase $\varphi_f[q(\varphi)]$ for a distribution $q(\varphi)$ that each agent may estimate independently. We find that the effective phases φ_f of each agent A and B closely agree.

In Sec. II, we define a simplistic phase-reduction [19] dynamics and our statistical sampling methods. In Sec. III, we demonstrate the quantitative convergence of different initial distributions to a single one. In Sec. IV we give an explicit example of a workable $\varphi_f[q(\varphi)]$ and show the strong agreement attainable between the φ_f 's of agents A and B. In Sec. V, we note the limitations of our study and argue for the generality and usefulness of this effective stochastic synchronization mechanism.

II. PRELIMINARIES

A. Impulsive perturbations as phase maps

Noise-induced synchronization occurs for independent agents with identical clocks. For our purposes, a clock is a nonlinear dynamical system orbiting a stable limit cycle. To illustrate stochastic synchronization, we specialize to a class of noise consisting of discrete, identical impulses (kicks) occurring at random times. The kicks are such that the oscillator remains within the basin of attraction of the limit cycle, whenever it occurs.

The effect of a kick on the clock can be compactly expressed via a phase-reduction prescription [19]: The oscillator traces a periodic loop in its dynamical manifold with a period T . We may label the points on this loop by a “phase position” φ ranging from 0 to 1, with a designated point assigned as the phase origin $\varphi \equiv 0$. Other points are assigned phase values equal to the time Δt required for the oscillator to reach them from the phase origin: $\varphi \equiv \Delta t/T$. This construction is equivalent to finding the action-angle variables in Hamiltonian mechanics [24]. Thus, the phase of an oscillator that started at $\varphi^{(0)}$ advances at a constant speed, $\varphi^{(0)} + t/T$, where mod 1 is implied in any algebraic operation over the phases.

Every kick to an oscillator creates a fixed long-term shift in its time-dependent phase compared to the state of the oscillator if there had been no kick. This shift depends on the oscillator’s phase position φ' at the moment of the kick. All effects described below result from the rearrangement of the oscillator positions due to this position-dependent shift. For impulsive kicks, it suffices to know the shift of an oscillator kicked at φ' , relative to the phase of an un-kicked oscillator that was at the phase origin at the moment of the kick. This shifted phase, denoted ψ , is illustrated in Fig. 1. Since all phase points move around the orbit at the same constant

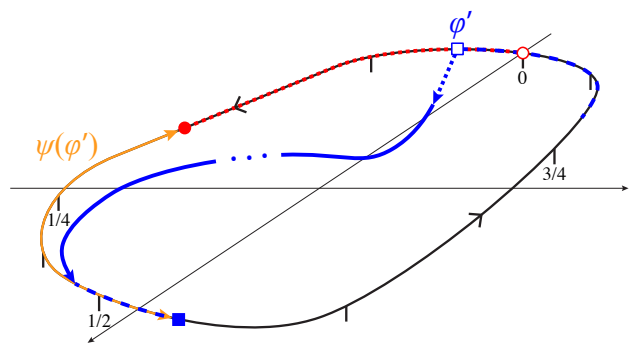


FIG. 1. Illustration of a phase map $\psi(\varphi)$ determination for a given limit cycle. A toy dynamical system is considered whose limit cycle is depicted by the closed black line in some dynamical phase space. Phase-position labels φ along the loop are marked for the assigned phase origin $\varphi = 0$ and for phase positions displaced by $1/4$, $1/2$, and $3/4$ cycle from this origin. An open square marks the phase position of the oscillator at a moment of a kick, when its phase position was φ' . The subsequent trajectory of this oscillator is sketched in blue, showing its departure from the limit cycle and its eventual return to it. Before and after the kick, the oscillator gains phase at a constant speed (along the dashed trajectories). Also shown (in red) is the unperturbed trajectory of an oscillator which was at the phase origin at the moment of the kick. The position of the kicked trajectory at some arbitrary later time is marked with a filled square. The position of the un-kicked trajectory at this same moment is marked with a filled circle. Since both trajectories advance around the loop at the same rate, their phase difference, indicated in orange, is independent of time. This difference for the arbitrary kick position φ' is defined as the phase map, $\psi(\varphi')$.

speed, the phase difference ψ for a given oscillator remains constant until the next kick. Evidently, if the kick has a negligible effect, the phase of an oscillator—initially equal to φ —remains so, and thus $\psi(\varphi) = \varphi$. Otherwise, the “phase map” function $\psi(\varphi)$ encodes the complete information about the effect of the perturbation.

A unique phase map $\psi(\varphi)$ can be determined for a given pairing of a dynamical system and a specified kick, as illustrated in *SI Appendix*, Sec. S2 [25, 26]. In biological contexts, $\psi(\varphi) - \varphi$ is called the phase response curve, quantifying the response of circadian clocks [2, 27] and neural networks [28] to environmental changes. In these cases, the clocks are a living organism and firing neurons, and the perturbations can be sporadic light impulses or shot noise from sensory neurons.

We study the case where this deterministic perturbation $\psi(\varphi)$ is applied at random times.¹ For simplicity, we may capture the effect of a k 'th kick by observing the oscillators at an integer number of cycles after the latest kick. The un-kicked position of the phase origin has continued its periodic motion and thus returns to the phase origin at such a moment. Likewise, the same phase is observed for the kicked oscillator after

¹ We assume that the waiting times in between kicks are sufficiently long so the oscillators have relaxed back to the limit cycle. For the case of possibly insufficiently-long times, see Ref. [29].

each completed cycle; we denote this phase as $\varphi^{(k)}$. Thus, the phase-map shift $\psi(\varphi')$ from the unkicked phase origin is simply $\varphi^{(k)}$. To complete the iteration, we must express the phase position at the moment of the k th kick φ' in terms of the previous kick's phase $\varphi^{(k-1)}$. During the random waiting time between the $k-1$ 'st and the k 'th kick, the oscillator has gained a phase that we denote by $\beta^{(k)}$. Thus, $\varphi' = \varphi^{(k-1)} + \beta^{(k)}$. Combining, we infer the effect of a single iteration,

$$\varphi^{(k)} = \psi(\varphi^{(k-1)} + \beta^{(k)}). \quad (1)$$

Due to the mod 1 constraint, only the fractional part of the waiting time in between kicks matters, which we denoted $\beta^{(k)}$. For simplicity, we assume that $\{\beta^{(1)}, \beta^{(2)}, \dots\}$ are identical independent uniformly-distributed random phases, $\beta^{(k)} \in [0, 1)$. Eq. (1), therefore, amounts to a Markov dynamics in the discrete “time” k , controlled by the phase map $\psi(\varphi)$ and the drawn $\beta^{(k)}$'s. Below, we compare the fates of two ensembles of oscillators exposed to the same sequence of $\beta^{(k)}$'s.²

Our aim in this paper is to examine generic behaviors of smooth phase maps. Accordingly, we consider simple cubic maps of the form

$$\psi(\varphi) = \varphi + A\varphi(1/2 - \varphi)(1 - \varphi), \quad (2)$$

where the “gain parameter” A determines the strength of the perturbations; when $A = 0$, $\psi(\varphi) = \varphi$, so the kick has no effect. We plot this $\psi(\varphi)$ for $A = 9.32$ in *SI Appendix*, Fig. S4, solid red curve. For completeness, we have repeated all the paper's quantitative analyses also for the quintic phase map, $\psi(\varphi) = \varphi + A'\varphi(1 - \varphi)(\Psi_1 - \varphi)(\Psi_2 - \varphi)(C - \varphi)$, where $C = (1 - \Psi_1)(1 - \Psi_2)/[\Psi_1\Psi_2 + (1 - \Psi_1)(1 - \Psi_2)]$ is such that $(d\psi/d\varphi)|_{\varphi=1} = (d\psi/d\varphi)|_{\varphi=0}$. We will show the results for the cubic phase maps; we observed that the same conclusions apply to the quintic ones.

B. Lyapunov exponent and synchronization

With maps of this form, strong perturbations will typically be characterized by an increased gain parameter A . Once perturbed, the quantity $|d\psi/d\varphi|$ measures the degree of spreading of a local interval around φ . This “spreading factor” therefore is closely related to the (in)ability of the phase map to synchronize adjacent phases. Hence, a measure of effective strength of the kicks can be formulated by averaging this spreading factor. Accordingly, we define Λ — the average of the log-spreading factor,³

$$\Lambda = \int_0^1 d\varphi \ln \left| \frac{d\psi}{d\varphi} \right|. \quad (3)$$

² We stress that all synchronization phenomena discussed in our work do not originate from phase distributions $q^k(\varphi)$ generated by an ensemble of noise histories $\{\beta^{(k)}\}$'s, but rather from the deterministic dynamics arising from a fixed history $\{\beta^{(k)}\}$ for an ensemble of initial states.

³ The integration measure is uniform since the waiting times are distributed uniformly $\beta \in [0, 1)$. Therefore, every oscillator is likely to experience a kick with equal probability everywhere along the phase circle.

This is the average Lyapunov exponent [17, 21] of the effective discrete-time dynamics in Eq. (1).

Phase maps with $\Lambda < 0$ tend on average to condense the phases. This means that oscillators that were subjected to the external force at common random waiting times $\beta^{(k)}$ are guaranteed to synchronize [17, 21]. On the other hand, $\Lambda > 0$ suggests that neighboring oscillators tend to spread apart in phase within successive kicks. This means that oscillators subjected to such forcings are guaranteed to not asymptote to a synchronized state in general. Increasing the gain parameter A ultimately causes Λ to cross the threshold from negative to positive. This threshold distinguishes “mild” from “strong” perturbations.

C. Probability distributions

In order to analyze the stochastic states encountered with positive Λ , we now consider the probability distribution $q^{(k)}(\varphi)$ arising from an initial $q^{(0)}(\varphi)$. The evolution of this $q(\varphi)$ can be directly inferred from that of individual phases φ in Eq. (1).

Prior to the perturbation, the phase distribution remains unchanged up to rotation: $q^{(0)}(\varphi - t/T)$ (see illustration in *SI Appendix*, Fig. S1). We apply the same forcing (phase map ψ) after waiting times $\{\beta^{(k)}\}$ common to all oscillators. After the k 'th kick, the ensemble will adopt the distribution $q^{(k)}(\varphi)$ according to

$$q^{(k)}(\varphi) = \int_0^1 d\varphi' q^{(k-1)}(\varphi') \delta(\varphi - \psi(\varphi' + \beta^{(k)})). \quad (4)$$

For $\Lambda < 0$, synchronization manifests in a very narrow, unimodal (“single-peaked”) $q^{(k)}(\varphi)$'s which will only get narrower on average. In contrast, for $\Lambda > 0$ one finds that $q^{(k)}(\varphi)$ continues to change erratically with each kick, with no ultimate convergence to narrow distributions. In Fig. 2, we show the typical evolution of two distributions under $\Lambda < 0$ and $\Lambda > 0$.

We use Eq. (4) to follow the evolution of $q_A^{(k)}(\varphi)$ and $q_B^{(k)}(\varphi)$ for agent A and B. They start from different initial phase distributions $q_A^{(0)}(\varphi)$ and $q_B^{(0)}(\varphi)$, but both are subjected to the same phase map and sequence of kick timings $\{\beta^{(k)}\}$.

In Sec. III, we show that after sufficiently many kicks, the two distributions become equal. This means that the same information is shared among the two agents, as both oscillators eventually follow the same statistics. To characterize this equivalence, we use the Kullback-Leibler divergence (KLD) [30] — a natural means of quantifying the divergence of the distribution $q_A(\varphi)$ from $q_B(\varphi)$,

$$D(A||B) \equiv \int_0^1 d\varphi q_A(\varphi) \ln \frac{q_A(\varphi)}{q_B(\varphi)}. \quad (5)$$

It quantifies the excess information stored in q_B when q_A is the presumed distribution. If the two distributions are the same, $q_A(\varphi) = q_B(\varphi)$, then $D(A||B) = 0$. Otherwise, $D(A||B) > 0$. We take $D(A||B) \rightarrow 0$ to mean that the two distributions have converged and become equivalent.

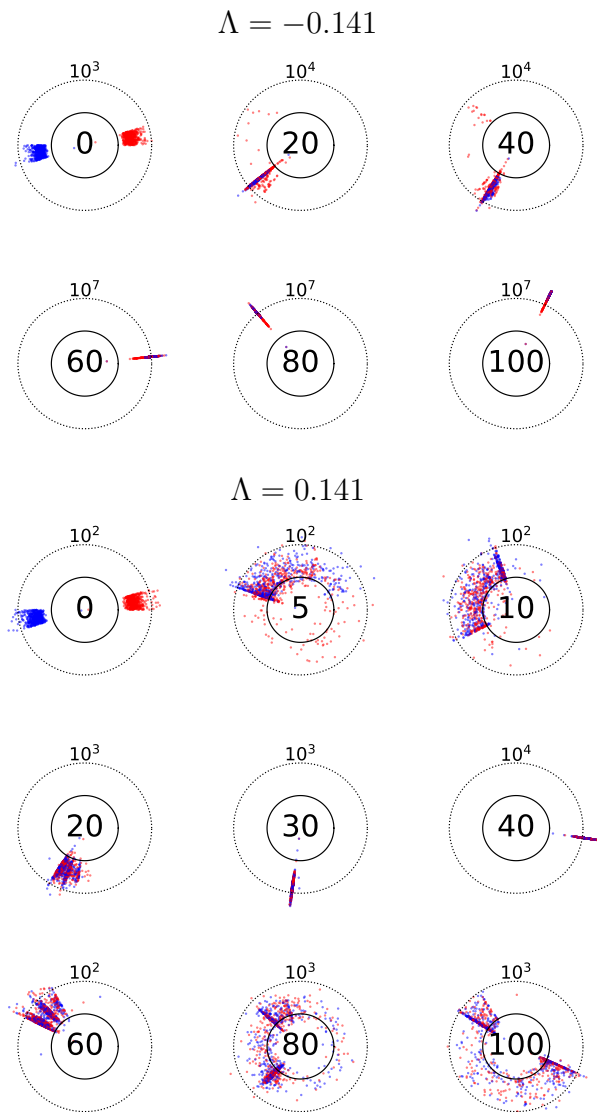


FIG. 2. A sequence of two, initially-different phase distributions $q_A^{(k)}(\varphi)$ (red) and $q_B^{(k)}(\varphi)$ (blue) subjected to common noise in a typical realization of Eq. (1) and Eq. (2) with either $\Lambda = -0.141$ ($A = 7.32$) or $\Lambda = 0.141$ ($A = 9.32$), as indicated. The initial distributions are uniform, $\varphi \sim U[0.0, 0.05]$ and $\varphi \sim U[0.5, 0.55]$, respectively. The distributions are shown on a circle so the periodicity mod 1 of the phase circle is apparent. The radial axis shows the distributions' values $q(\varphi)$ on a log scale, where $q(\varphi) = 1$ for the inner full circle and as indicated for the outer dotted circles. The kick numbers k are shown inside the inner circle. The $\Lambda < 0$ dynamics are synchronizing, so their distributions become centered around the same phase value and their width decreases over time on average. For $\Lambda > 0$, the distributions evolve erratically. However, remarkably, the red and blue points co-locate; they converge unto the same sequence of sharply-multimodal distributions under common noise—this is the central finding of our work. The distributions are sampled by tracking $N = 500$ initial phases via the nearest-neighbor distances; see Eq. (A1). The entropies of the two distributions and the KLDs among them are shown in Fig. 3 for $\Lambda = 0.141$ and *SI Appendix*, Fig. S6 for $\Lambda = -0.141$. A detailed view of the blue distribution at $k = 100$ for $\Lambda = 0.141$ is shown in *SI Appendix*, Fig. S7.

Pursuing this evidence that all agents become statistically equivalent, we show in Sec. IV that each agent may define an effective phase that agrees closely with that of the other agent. This is possible in spite of the agents' current phases differing widely. This agreement is possible owing to the special behavior of phase maps close to the $\Lambda = 0$ threshold. Their typical $q(\varphi)$ distributions are strongly ordered, consisting of few narrow peaks, as will be seen below. To quantify the degree of order in a distribution we use the information entropy S [30] defined in our context by

$$S \equiv - \int_0^1 d\varphi q(\varphi) \ln q(\varphi). \quad (6)$$

The highest possible value $S = 0$ is achieved only for the uniform phase distribution, $q(\varphi) = 1$, while sharp multimodal (“multi-peaked”) distributions will have a strongly-negative entropy. From a thermodynamic perspective, changes in the entropy are a lower bound on the work needed to create the given ordered distribution from a fully random (uniform) one.

The convolution of Eq. (4) cannot be solved analytically. Instead, we implement Eq. (4) numerically by representing each $q^{(k)}(\varphi)$ as a sampling of N discrete phases $\{\varphi_1^{(k)}, \dots, \varphi_N^{(k)}\}$, which by construction follow Eq. (1). This set of phases is used to estimate the entropies [31] and KLDs [32]. The details of the numerical estimators can be found in Sec. A1. The numerical errors in their estimations for the samples sizes considered here are $\Delta S \sim 0.2$ and $\Delta D \sim 0.05$.

III. CONVERGENT DISTRIBUTIONS

The synchronization scheme proposed in Sec. IV requires that $q_A^{(k)}$ and $q_B^{(k)}$ converge to the same distributions as $k \gg 1$. In this section, we demonstrate this convergence quantitatively via the decay of the KLD to zero for $\Lambda > 0$.

To this end, we simulate two oscillator ensembles, each consisting of $N = 500$ phase samples. Their phase values are randomly and independently selected from different uniform distributions; $\{\varphi_A^n \sim U[0, u]\}$ for the sender and $\{\varphi_B^n \sim U[0.5, 0.5 + u]\}$ for the receiver. By this, we study the extreme case of well-separated (non-overlapping) initial phase distributions. We subject the oscillators to Eq. (1) for given Lyapunov exponents Λ and initial widths u . All $2N$ phases evolve under the same $\psi(\varphi)$ and uniformly-distributed waiting times $\{\beta^{(k)} \sim U[0, 1]\}$. At each kick, we estimate $S_A^{(k)}$, $S_B^{(k)}$, $D^{(k)}(A||B)$, and $D^{(k)}(B||A)$.⁴

For completeness, in *SI Appendix*, Sec. S5 we show how the synchronization for $\Lambda < 0$ manifests in the entropy (cf. also Ref. [21]) and the KLD. The KLD has not been considered

⁴ The KLD is not symmetric. However, since the initial distributions are offset by exactly half of the phase circle and $\beta \in [0, 1)$, we expect both $D^{(k)}(A||B)$ and $D^{(k)}(B||A)$ to have the same statistics over many repetitions. Indeed their averages of many realizations, depicted in Fig. 4(a,b), are equal.

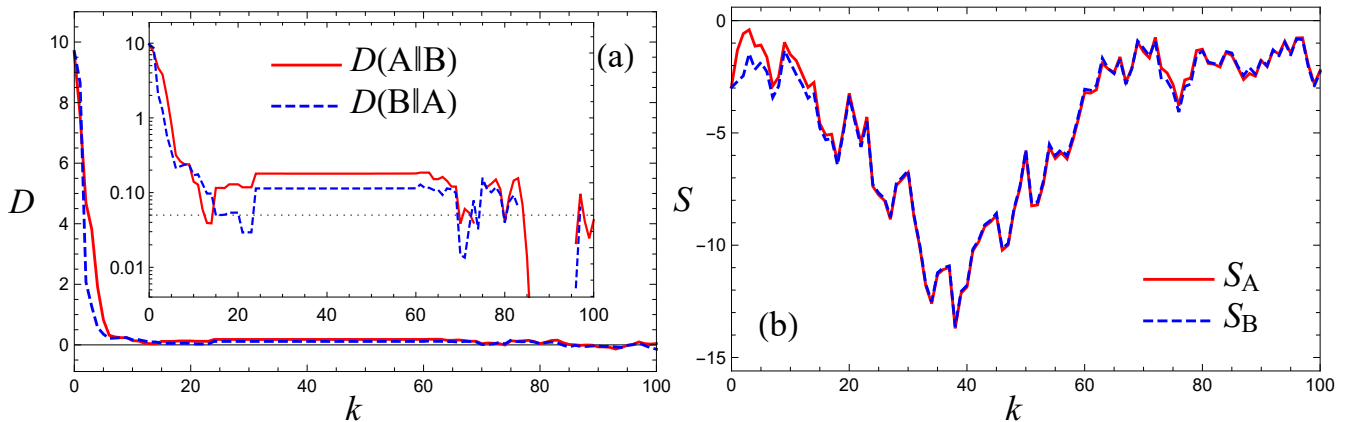


FIG. 3. (a) Kullback-Leibler divergences (KLDs) $D(A||B)$ and $D(B||A)$ among two distributions and (b) entropies S_A and S_B of each distribution, as obtained for the waiting time realization $\{\beta^k\}$ of Fig. 2 with $\Lambda = 0.141$. Inset: The KLDs on a log-scale, where the numerical error in the KLD's estimation is indicated by the horizontal dotted line. The number of phase samples is $N = 500$. Both initial distributions are of width $u = 0.05$. The numerical errors in the estimation of the KLDs and entropies are $\Delta D = 0.05$ and $\Delta S = 0.2$, respectively.

previously in the literature, as only a single ensemble has been considered until present.

For $\Lambda > 0$, the two distributions $q_A^{(k)}(\varphi)$ and $q_B^{(k)}(\varphi)$ change erratically between consecutive kicks, *e.g.*, as peaks are formed at phase values in the vicinity of the phase map's extrema, and 'smeared' away from them (see Fig. 2 and *SI Appendix*, Fig. S4). Accordingly, in Fig. 3(b), we see that the entropy also changes chaotically [21]. At the same time, remarkably, both KLDs decay to zero as seen in Fig. 3(a), indicating that the two ensembles eventually converge to the same distribution.⁵ Accordingly, the entropies of both distributions coincide at later times in Fig. 3(b). Note that a different realization of waiting times $\{\beta^{(k)}\}$ would produce vastly different distributions (see *SI Appendix*, Fig. S5); what we report, therefore, is that the two agents' distributions agree more closely with more kicks for every stochastic realization.

We qualitatively understand this ensemble convergence as arising from independence of initial state. After many kicks, Eq. (1) approaches a chaotic map from the phase circle onto itself with Lyapunov exponent Λ per kick. Consider the map from an initial phase $\varphi^{(0)}$ to the final phase $\varphi^{(k)}$ for a particular sequence of random and uniformly-distributed waiting times $\{\beta^{(k)}\}$. This map comes from a statistically uniform sampling of the phase map $\psi(\varphi)$ and has an overall Lyapunov exponent for any $\varphi^{(0)}$ that approaches $k\Lambda$. Any such map fully mixes all $\varphi^{(0)}$ s [33]. That is, the $\varphi^{(k)}$ for a given $\varphi^{(0)}$ may be arbitrarily close to the $\varphi'^{(k)}$ for other $\varphi'^{(0)}$'s residing anywhere throughout the phase circle. Thus, any uncertainty in an observed $\varphi^{(k)}$ erases all knowledge of $\varphi^{(0)}$. So, we expect that for a given uncertainty in $\varphi^{(k)}$ there exists some

kick number K_m such that any dependence of $\varphi^{(k)}$ on $\varphi^{(0)}$ for $k > K_m$ is undetectable. This diminishing uncertainty manifests, therefore, in a KLD that approaches zero, implying that the two distributions differ only by this decaying uncertainty. We proceed to study the rate with which the oscillators become statistically indistinguishable.

A. Convergence rate

Fig. 3 is a single realization of stochastic waiting times $\{\beta_k\}$. To find the typical time K_m that the agents should wait until their distributions become similar, we simulate a larger sampling of KLDs. To observe as many reliable KLD values as possible prior to their decay below the numerical-error cutoff of $\Delta D = 0.05$, we picked the two initial distributions to be of width $u = 10^{-4}$, so they are far apart and very narrow. We simulate 500 realizations of $D^{(k)}(A||B)$ and $D^{(k)}(B||A)$ dynamics, each repetition sampling the above initial distribution and picking $\{\beta^{(k)}\}$ anew. We plot, as an illustration, the average KLDs and their statistical uncertainty versus k for $\Lambda = 0.405$ in Fig. 4(a) and $\Lambda = 0.121$ in Fig. 4(b).

For all Λ 's, we observe a predominant regime of an exponential decay with k , shown with a dashed orange lines in Fig. 4(a,b).⁶ The decay is to be expected due to the stochastic evolution of the distributions, which are mixed until becoming equivalent. This exponential decay is typically cleaner for higher Λ 's (compare $k \in (10, 45)$ in Fig. 4(a) with $k \in (70, 250)$ in Fig. 4(b)), and lasts until we reach the numerical error cutoff for the KLD estimator, ~ 0.05 .

⁵ The brief transient during $25 \lesssim k \lesssim 65$, where the KLD seems to stay at a constant value is a result of the distributions being very narrow at these time steps (see Fig. 2), so they change widths together without affecting the KLD. We quantitatively explain this behavior in *SI Appendix*, Sec. S5. When the distribution widen afterwards, the KLD decreases to below its numerical error cutoff.

⁶ The true KLDs should have started from ∞ (as the two initial distributions are nonoverlapping), but instead they begin at a large finite value, $D^{(0)} \simeq 15.1 \sim -\log u$. This is an artifact of the numerical KLD estimate [32] (Eq. (A3)), and thus the KLD values at the first few kicks in Fig. 4 should be taken with caution. The exponential decay due to mixing begins past that transient.

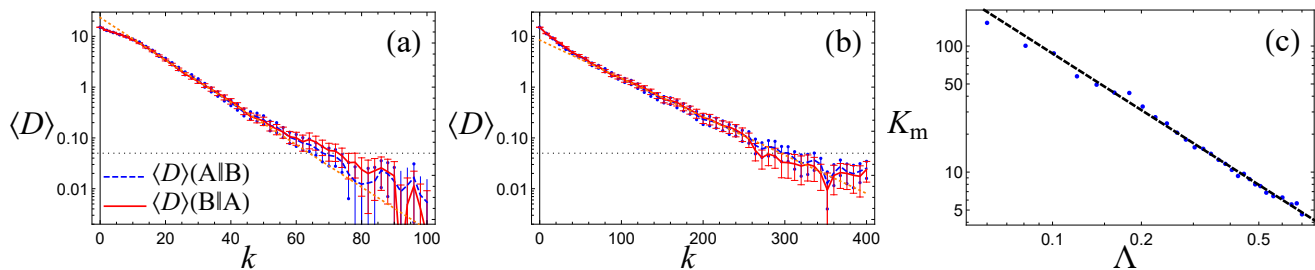


FIG. 4. The average Kullback-Leibler divergence (KLDs) $D(A||B)$ and $D(B||A)$ among the two distributions, averaged over 500 waiting-time realizations. We used phase maps of Eq. (2) with various values of Λ obtained by varying the gain parameter A . We show the results for (a) $\Lambda = 0.405$ and (b) $\Lambda = 0.121$. The number of phase samples is $N = 500$ in each ensemble, and they are initially uniform-distributed with width $u = 10^{-4}$. Dashed orange lines depict the exponential fit from which we extract the mixing-kick number. (c) The mixing-kick number K_m versus Lyapunov exponent Λ . K_m is identified as minus the inverse slope in the exponential decay of $\langle D \rangle$. The exponential regime begins after a transient where the distributions spread and overlap, and terminates when the KLD is comparable with its numerical estimation error, ~ 0.05 . Mixing occurs faster as Λ increases, so the two agents typically converge earlier. The decay is the powerlaw $K_m = 2.82\Lambda^{-1.49}$.

For each Λ , we fit an exponential (as in Figs. 4(a,b)) to obtain a decay rate defined as $1/K_m(\Lambda)$. We interpret these K_m 's as the mixing-kick number. We verify for various Λ 's that it does not depend on the initial condition (by simulating $u = 5 \cdot 10^{-4}$ as well) or the sample size (by simulating $N = 100$, too); $K_m(\Lambda)$ remained identical within 3% (not shown) for each Λ . This supports our claim that the decay is predominantly exponential, and suggests that our choice for the mixing-kick number is meaningful as it is only a property of Λ and is independent of the numerical limitations for the class of phase maps studied.

In Fig. 4(c) we plot the mixing-kick number K_m versus Λ . As expected, the more violent the phase map (bigger Λ) the faster the mixing. We find numerically that the dependence of K_m on Λ is consistent with a power law, $K_m(\Lambda) \sim \Lambda^{-1.491 \pm 0.046}$. We caution that the exponential fit for the decay of the KLD with low Λ is not perfect (specifically, for $\Lambda \lesssim 0.2$), so their K_m should be taken with a grain of salt. The exact functional form of $K_m(\Lambda)$ is not central to what follows; we shall only use the fact that K_m decays with Λ as a qualitative guide. The power-law does give the expected limiting behavior, *viz.*, $K_m(\Lambda \rightarrow 0^+) \rightarrow +\infty$.

To summarize, for $\Lambda > 0$, the two phase statistics become identical after iterating sufficiently longer than the mixing-kick number K_m , which is shown to decay as a power law with Λ . Thus, for the purpose of establishing synchronization, we will first make the reasonable assumption that both agents have received a number of noisy kicks exceeding an agreed threshold. In the next section we demonstrate this synchronization.

IV. EFFECTIVE SYNCHRONIZATION

In Sec. III, we found that agents A and B must eventually share $q^{(k)}(\varphi)$ in both the $\Lambda < 0$ (synchronizing) and the $\Lambda > 0$ (unsynchronizing) regimes. With $\Lambda < 0$, the two agents agree at every moment (sufficiently-long after the most recent kick) on a specific phase to experimental accuracy [15] and can use it to perform simultaneous actions or

communicate. For $\Lambda > 0$, while the resultant distributions do not asymptotically approach a sharp peak, the distributions of two agents become fully identical as captured by the approach of the KLD among them to zero. The synchrony in the former and convergence in the latter remain with arbitrarily more kicks. Thus, any functional of $q(\varphi)$ calculated independently by both agents would be shared after any large k . Below we consider a functional we refer to as the ‘‘fiducial phase’’, $\varphi_f[q(\varphi)]$, that indicates a virtual phase position upon which both agents must agree at a given moment.

Given the value of $\varphi_f^{(k)} = \varphi_f[q^{(k)}(\varphi)]$ after a kick, any agent can infer its value at a later time $\varphi_f^{(k)} + t/T$ from its own phase at that moment, as it has also advanced from $\varphi_n^{(k)}$ to $\varphi_n^{(k)} + t/T$. Since the kicks occur at common timing, the time t that has passed after the kick is the same for all agents, and hence any difference between their current $\varphi_f^{(k)} + t/T$'s is the same as the difference between their initial $\varphi_f^{(k)}$'s, $[\varphi_{f,A}^{(k)} + t/T] - [\varphi_{f,B}^{(k)} + t/T] = \varphi_{f,A}^{(k)} - \varphi_{f,B}^{(k)}$. Thus, if the prescription for $\varphi_f^{(k)}$ is such that $\varphi_{f,A}^{(k)} \simeq \varphi_{f,B}^{(k)}$, their $\varphi_f^{(k)} + t/T$'s are also about equal. The two $\varphi_f^{(k)} + t/T$ are thus effectively synchronized over time; see illustration in *SI Appendix*, Fig. S1. We demonstrate below that this type of synchronization can indeed be achieved.

The uncertainty in φ_f must depend on the degree of nonuniformity of $q(\varphi)$; surely, no φ_f can be unambiguously determined if $q(\varphi)$ is completely uniform. Further, uncertainty in measuring $q(\varphi)$ leads to further uncertainty in φ_f . Below we test the discrepancy between $\varphi_{f,A}$ and $\varphi_{f,B}$ using the finite sampling method employed above. Our proof-of-concept example below shows that with a fixed sample size N , it is indeed feasible to attain arbitrarily-small discrepancies which further decrease with bigger N . These discrepancies depend strongly on the nonuniformity of the $q(\varphi)$ at hand, as measured by its entropy, Eq. (6). Thus, reliably small discrepancies require phase maps $\psi(\varphi)$ with small typical entropies.

Here we follow a simple strategy to arrive at a choice of fiducial phase, φ_f , for a given $q(\varphi)$. We seek a functional that is defined to high precision when the $q(\varphi)$ is strongly nonuni-

form and concentrated into narrow peaks (cf. Fig. 2). If there is a single peak, an obvious choice for φ_f is simply the position of the maximum. If there are two or more maxima, one generally dominates over the other in the sense that it has the greatest height and covers more probability mass. This suggests a choice of φ_f as the position of the highest peak.

To determine a peak position, one needs a smooth estimate of $q(\phi)$ from the sampled values $\{\varphi_1, \dots, \varphi_N\}$. We obtain an estimate denoted $Q(\varphi, \sigma)$ smoothed to a “bandwidth” σ using the method of kernel-density estimation [34–36], detailed in Sec. A 2. The reliability of the φ_f obtained depends on σ . Large σ produces a $Q(\varphi; \sigma)$ with a few broad peaks whose positions have high uncertainty, whereas small σ gives numerous statistically insignificant peaks; see illustration in *SI Appendix*, Figs. S7.⁷

We observe that the multimodal distributions encountered for small positive Λ have a dominant peak containing a substantial fraction of the N samples (Fig. 2). In these narrowly-peaked distributions, the measured entropy S (Eq. (6) and Eq. (A2)) gives guidance about the appropriate σ : If all $\{\varphi_n\}$ ’s lie within an interval of width w , then $S = \ln w$ up to an additive constant [41]. Now, if instead a substantial fraction of them lie within w , the entropy remains comparable to $\ln w$. Thus, the measured entropy for each $q(\varphi)$ gives a characteristic length indicative of the dominant peak’s width. Thus, in what follows, we have simply used a bandwidth σ equal to this w , *i.e.*, $\sigma = e^S$, as the peak center will not be offset by more than its width. We explored other choices of σ empirically to see their effect on the resulting uncertainties in φ_f ; see *SI Appendix*, Figs. S7 and S8. Accordingly, our fiducial phase of choice is

$$\varphi_f = \operatorname{argmax}_{\varphi \in [0,1]} Q(\varphi; e^S). \quad (7)$$

This crude choice turns out to be sufficient for our purpose.

A. Proof of effective synchronization

We now test the extent to which agent A’s $\varphi_{f,A}^{(k)}$ and B’s $\varphi_{f,B}^{(k)}$ agree. We use an extensive simulation of the phase map of Eq. (2) with $\Lambda = 0.141$ and $N = 500$. We extend the simulation depicted in Fig. 2 to a large number of kicks, $k = 10^4$. For every k , using the procedure of Sec. A 2 (Eq. (7)), we find $\varphi_{f,A}^{(k)}$ and $\varphi_{f,B}^{(k)}$. To quantify the success of our scheme for identifying a common fiducial phase, we consider the statistics of the deviation $\Delta\varphi_f = \varphi_{f,A} - \varphi_{f,B}$. There are indeed 4,987 positive and 5,013 negative $\Delta\varphi_f$ values, both exhibiting identical histograms (the KLD among the two $\ln(\pm\Delta\varphi_f)$ distributions is $\mathcal{O}(10^{-3})$), so we only show $|\Delta\varphi_f|$ henceforth. Likewise, in light of the convergence we observe in Sec. III, we shall only plot $S = (S_A + S_B)/2$, where S_A and S_B only differ by numerical entropy estimation error ~ 0.2 for large $k \gg K_m$.

Though $\Delta\varphi_f$ varies widely between kicks, this variability stems from the erratically varying entropies of the distributions $q^{(k)}$ (Fig. 3(b)). In Fig. 5(a), we plot the scaled deviation $\ell \equiv \sqrt{N}|\Delta\varphi_f|/e^S$ versus S , where the color intensity depicts the joint probability density for $(S, \log_{10} \ell)$. We see that for all S ’s, most $|\Delta\varphi_f|$ ’s lie close to e^S/\sqrt{N} (see the $\ell = 1$ line). The deviations from the peak appear to fall off roughly as a Gaussian—we further resolve this in Fig. 5(b). There, we plot the marginal cumulative distribution of the rescaled deviation ℓ irrespective of S , highlighting the abundance of small deviations as seen qualitatively in Fig. 5(a). The inset shows the marginal cumulative distribution of the entropy S irrespective of ℓ . The raw data for Fig. 5—the 10^4 instances of deviations $|\Delta\varphi_f|$ versus S —is shown in *SI Appendix*, Fig. S8(a).

Overall, both panels of Fig. 5 are most encouraging, as a common fiducial phase is established within uncertainty much less than 1. Indeed the most abundant instances surrounding the black point ($\ell \simeq 1.0$, $S \simeq -2.0$) have a phase discrepancy of order $|\Delta\varphi_f| = 1 \cdot e^{-2}/\sqrt{500} = 6.1 \cdot 10^{-3}$, which is the fraction of a percent synchronization accuracy we report. Further, much smaller deviations are abundant: From Fig. 5(b), 10% of the distributions produce reduced discrepancies smaller than $\ell = 10^{-1}$, or $|\Delta\varphi_f| = 6.1 \cdot 10^{-4}$. The fitted error function ($\operatorname{erf}(x) = (2/\pi) \int_0^x dt e^{-t^2}$) suggests that the discrepancy predominantly follows a normal distribution. This supports our proposed scaling $|\Delta\varphi_f| \sim e^S/\sqrt{N}$, as indeed the predominant peak typically contributes most to the entropy, so the local width is comparable to e^S and contains most of the phase samples ($\mathcal{O}(N)$), so the standard deviation in the estimation of the mean decays as $1/\sqrt{N}$.

Repeating the above for $\Lambda = 0.101, 0.141, \dots, 0.501$ reveals that the entropy is still exponentially distributed with a (negative) mean that increases with Λ , asymptoting to 0 for large Λ , which is consistent with Ref. [21]. For all Λ ’s tested and for $N = 125, 250, 500$, all the corresponding plots fully overlap with Fig. 5(b) (except for the statistically insignificant tails $\ell < 10^{-2.5}$).

To conclude, this section has provided concrete evidence supporting the proposal made in Sec. I. Identical nonlinear oscillators exposed to identical noise can enable independent agents to act in concert and perform time-based communications as though their clocks were synchronized, even though they are not and their phases are only statistically determined.

V. DISCUSSION

In this paper, we showed that noise-induced synchronization can be extended beyond its recognized limits. Our study demonstrated effective synchronization under noise-driven dynamics with positive Lyapunov exponents, which precludes conventional noise-induced synchronization. This effective synchronization arose from two key features of our dynamics. First, the statistical distribution of phases at a given moment becomes independent of the initial distribution for every realization of waiting times, as noted in Sec. III. Thus, the distributions seen by two independent agents become equal to each other while varying (together) strongly with more kicks. Sec-

⁷ Finding an optimal bandwidth σ , particularly for highly-multimodal distributions, is an open question in the field [37–40].

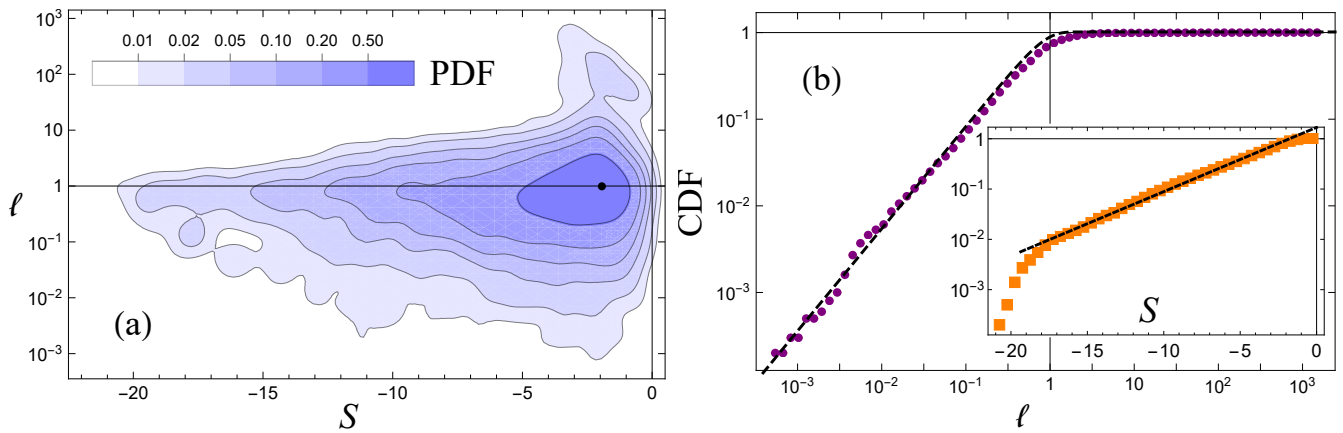


FIG. 5. (a) A density plot of the rescaled discrepancy, $\ell = \sqrt{N}|\Delta\varphi_f|/e^S$ versus $S = (S_A + S_B)/2$. The shade of blue represents the indicated values of the joint probability density function (PDF) to obtain S and $\log_{10} \ell$, relative to its maximum. It was computed with kernel-density estimation from the $k = 10^4$ data points shown in *SI Appendix*, Fig. S8(a), using a Gaussian kernel of width 0.4 in S and 0.2 in $\log_{10} \ell$. The maximal value is $\text{PDF}(-1.94, -0.0052) = 0.135$, whose position is indicated by the black point. The puzzling lobe of probability at the upper right is addressed in *SI Appendix*, Sec. S8. (b) The marginal cumulative distribution function (CDF) of the discrepancy $\log_{10} \ell$, which was arranged into bins of size 0.25. The dashed line is the error function of width unity; its close agreement with the data suggests that the discrepancy is predominantly normal-distributed with the expected scaling $|\Delta\varphi_f| \sim e^S/\sqrt{N}$. Inset: The marginal CDF of the entropy S , which was arranged into bins of size 0.5. The dashed linear line implies, up to the low- and high-entropy outliers, that the entropy is exponentially distributed [21].

ond, concentrating on dynamics whose Lyapunov exponent is small in magnitude, we found in Sec. IV that the prevalence of low-entropy distributions $q(\varphi)$ permits accurate effective synchronization.

In this section, we assess the potential impact of these results. First, we note the narrow though significant scope of our explicit study. We argue that this generalized synchronization should occur generically for oscillators subjected to non-synchronizing noise, despite possible degrading effects we ignored. We then discuss the power-law trade-off we observed between the desirable rapid convergence and the obtainable precision of the generalized synchronization. Finally, we consider how generalized synchronization might be relevant for explaining forms of cooperative behavior in organisms.

A. Limitations

Our demonstration of effective synchronization was made in a narrow context. Among the various types of noise treated in the literature [15, 22], we considered only impulsive noise whose effect could be described by a phase map [19, 21]. Furthermore, the bulk of our study used a simple class of such maps — a cubic polynomials; other phase maps may not culminate in low-entropy distributions or a meaningful fiducial phase. Additional aspects we did not address include counter-effects that oppose synchronization, such as a disruptive noise that acts independently on each oscillator [17] and inevitable differences between the two agents' oscillators [16]. These degrading effects would surely reduce the degree of effective synchronization that we demonstrated, and may even render our procedure to determine an effective synchronized phase unstable.

These limitations mean that our example is not immediately applicable to realistic conditions. Still, we may argue that the effect is somewhat general and robust. The effective synchronization persists under continuous variation of the phase map $\psi(\varphi)$ through cubic and quintic phase maps and over a range of Lyapunov exponents Λ . Further, we recover the effective phase φ_f using standard-precision computations and conventional sampling methods. This is not a delicate effect analogous to time-reversing a chaotic trajectory. Moreover, all of our results in Sec. IV show a common variation with the distribution entropy S , $\Delta\varphi_f \sim e^S/\sqrt{N}$, under a range of underlying dynamics that gave rise to the distribution. Under general noise, one may define the Lyapunov exponent [15, 18], the distribution of φ values $q(\varphi)$ at a given time, the notion of independence of this $q(\varphi)$ on initial conditions, and the determination of a fiducial phase φ_f from a given $q(\varphi)$. Thus, the synchronization we found in our narrow context should plausibly have a counterpart for clocks subjected to more general forms of noise, such as sensory neural networks [28].

Although our prescription for identifying φ_f is somewhat ungainly, the result is about as precise as one might hope. The statistical fluctuations of $\Delta\varphi_f$ appear consistent with an N -sample average of a Gaussian distribution whose variance is of order $N\langle\Delta\varphi_f^2\rangle$, where $\langle\cdots\rangle$ denotes the average over samples. The entropy of the $\Delta\varphi_f$ distribution is thus of order $\ln(\langle\Delta\varphi_f^2\rangle^{1/2}) + \log N$ [41]. Now, the scaling shown in Fig. 5 amounts to saying $\ln(\langle\Delta\varphi_f^2\rangle^{1/2}) \simeq S - \log N$, i.e., S is comparable to the entropy of $\Delta\varphi_f$. Thus, a much more precise φ_f than the observed one would need to contain more information than the source distribution $q(\varphi)$ from which it was derived — a contradiction. Thus, we cannot expect other methods to yield qualitative improvements in precise synchronization compared to $\Delta\varphi_f \sim e^S/\sqrt{N}$. Instead, we can hope

for more insightful and efficient calculation methods, which might or might not involve a fiducial phase.

A clear practical limitation of our procedure was the laborious calculations it required. Partly, this labor was due to our choice to demonstrate precise synchronization, *i.e.*, small $\Delta\varphi_f$. This required using phase maps that produce low-entropy distributions (small positive Λ). This small $\Lambda > 0$ implies slow convergence of $q(\varphi)$, as shown in Sec. III. (For our example of Sec. IV, the convergence number K_m was about 10^2 ; knowledge of the last $\sim 10^2$ was needed in order to infer the converged φ_f .) If instead we had been content to show synchronization to only a few bits of precision, we could have relaxed our requirement of small entropy and small $\Lambda > 0$. Then, the large number of kicks needed to obtain a converged φ_f would be correspondingly reduced, thus reducing the required computation. We now consider further this tradeoff between computational labor and precision.

B. Convergence rate scaling

The central feature of our dynamics that makes effective synchronization possible is the property of convergence, as discussed in Sec. III; the final distribution $q(\varphi)$ depends only on the recent history. On the other hand, if the history required is long, one must take account of many kicks in order to determine the needed converged distribution—a lengthy process. Thus, it is important to know what governs the speed of convergence.

Our empirical study showed a simple behavior of the convergence though K_m —the number of kicks required for convergence to a common $q(\varphi)$. The qualitative trend was as expected: Larger (positive) Λ (thence larger typical entropy S) gave faster convergence. Our study showed an apparent power-law relation between K_m and Λ , *viz.*, $K_m \sim \Lambda^{-3/2}$. This robust behavior reinforces the overall consistency of our effective synchronization finding. From this formula, one can readily infer the increase in Λ needed to effect a desired reduction in K_m . Then, from $S \sim 1/\Lambda$ of Ref. [21] and $\Delta\varphi_f \sim e^S/\sqrt{N}$ from Sec. IV, one can infer the expected loss of precision in φ_f . It will be useful to demonstrate the scaling of K_m more generally and extensively.

C. Biological implications

We posit that this synchronization scheme could enable biological agents—cells, organelles, or gene expression networks—to cooperate in a wider range of noisy environments than previously envisioned. For example, our mechanism may be relevant to a long-standing experimental puzzle about information transmission between neurons via sequences of pulses or spikes [42]. The timing of these spikes is believed to carry that information [4]; thus, there needs to be some means of calibrating this timing. The present work suggests that the ambient electrical noise in the brain or variations of the sensed environment [5, 6, 28] could aid this calibration. In particular,

these effects may serve as sources for common noise, which can produce a generalized notion of synchronization.

VI. CONCLUSION

The mechanism we reported here is hardly a compelling explanation of neuronal information transfer and synchronized action among autonomous agents. Nonetheless, this mechanism shows an implicit organization, *i.e.*, synchronization, hidden in apparent chaos. Thus, it adds to the possible ways that evolved systems such as biological organisms might exploit complex dynamics to generate subtle, adaptive behavior. It seems worthwhile to explore such mechanisms further.

ACKNOWLEDGMENTS

We benefited from discussions with Efi Efrati and Colin Scheibner. We thank Chuanyi Wang for providing the efficient functional form of the quintic maps. We also thank Gil Ariel, Omer Granek, Andrej Košmrlj, Muhittin Mungan, Colin Scheibner, and Tony Song for helpful comments on the manuscript. B.S. acknowledges support from the Princeton Center for Theoretical Science. B.S. would like to thank the members of the James Frank Institute of the University of Chicago for their warm hospitality, where the research was initiated.

Appendix A: Materials and Methods

1. Binless estimation methods using samples

Here we explain how we estimate the phase distributions plotted in Fig. 2, and how we estimate the entropy and Kullback-Leibler divergence (KLD) throughout, using a finite number of samples N .

At every timestep in our simulations, we generated N phase samples per agent, $\{\varphi_{A1}^{(k)}, \dots, \varphi_{AN}^{(k)}\}$ and the same for B. To draw Fig. 2, we used the following simplistic estimate:

$$q_{An}^{(k)} \equiv q_A^{(k)} \left(\varphi = \frac{\tilde{\varphi}_{An+1}^{(k)} + \tilde{\varphi}_{An}^{(k)}}{2} \right) = \frac{1}{N} \frac{1}{\tilde{\varphi}_{An+1}^{(k)} - \tilde{\varphi}_{An}^{(k)}} \quad (\text{A1})$$

(and the same for $q_B^{(k)}$), where $\{\tilde{\varphi}_{An}^{(k)}\}$ are the instantaneous phase samples of agent A, $\{\varphi_{An}^{(k)}\}$, arranged in increasing order on a ring ($\tilde{\varphi}_{An+1}^{(k)} > \tilde{\varphi}_{An}^{(k)}$, with a mod 1 constraint) and $1/N$ ensures normalization. In Sec. IV, where a statistically significant estimate of $q^{(k)}(\varphi)$ was needed, we used, rather, the kernel-density estimate of Eq. (A4).

Given these samples, we used established methods [31, 32] of estimating the entropy and KLD. These approximations can be conveniently expressed in terms of the nearest-neighbor distances between pairs of phases. Consider the n 'th phase in ensemble A at iteration k ($\varphi_{An}^{(k)}$); it has a unique closest

distance to a phase in ensemble B, $\varphi_{Bm}^{(k)}$ (where m need not be equal to n). We denote the distance between these two as $\Delta_{An \leftarrow B}^{(k)}$. (By the same logic, we also denote $\Delta_{An \leftarrow A}^{(k)}$, $\Delta_{Bn \leftarrow B}^{(k)}$, and $\Delta_{Bn \leftarrow A}^{(k)}$.) Now, we estimate the entropy of agent A's distribution using [31]

$$S_A^{(k)} = \frac{1}{N} \sum_{n=1}^N \ln \Delta_{An \leftarrow A}^{(k)} + \ln(2N - 2) + \gamma \quad (\text{A2})$$

(and the same for S_B), and the KLD of distribution A from B using [32]

$$D^{(k)}(A \| B) = \frac{1}{N} \sum_{n=1}^N \ln \frac{\Delta_{An \leftarrow B}^{(k)}}{\Delta_{An \leftarrow A}^{(k)}} + \ln \frac{N}{N-1} \quad (\text{A3})$$

(and the same for $D^{(k)}(B \| A)$), where $\gamma = 0.577$ is the Euler-Mascheroni constant. See Fig. 3 and *SI Appendix*, Fig. S6 for a typical evolution of the entropy and KLD for $\Lambda = 0.141$ and $\Lambda = -0.141$, respectively.

There are two technical limitations involving the above binless estimation methods. First is our limited sample size $N = 500$, leading to an errorbar of ± 0.2 for entropy values (identified from samples of uniform distribution) and ± 0.05 for KLD values (identified from two sets of samples of the same Gaussian distribution). Second is the limited machine precision [21]; the phases are distinguishable only up to $\Delta_{An \leftarrow B}^{(k)} > 2^{-52}$ using the conventional 64bit representation of real numbers. Each sample with $\Delta_{An \leftarrow B}^{(k)} < 10 \times 2^{-52}$ is ignored, and we replace $N \rightarrow N - 1$.

The loss of samples to machine precision is a prevalent limitation. In the long realization ($k = 10^4$) of Sec. IV, 407 and 439 samples remained in the end for ensembles A and B, respectively, which means that our estimates are still statistically meaningful. On the other hand, this implies that the low-entropy distributions (which are those that usually culminate in loss of samples) did not appear much; see Fig. 5, where we see no distribution with $S < -21$. Upon continuing this simulation, there were no longer any distinguishable

phase samples past $k = 1.2 \cdot 10^4$, at which point the dynamics have attained entropies between $-34 < S < -21$. Were lower-entropy distributions to appear, our results of the main text would improve further, as they are particularly useful for having a small discrepancy $\Delta\varphi_f \sim e^S/\sqrt{N}$.

2. Identifying a fiducial phase

To obtain φ_f we must find a smooth estimate of $q(\varphi)$ from the sampled values $\{\varphi_1, \dots, \varphi_N\}$. For this purpose, we use the methodology of kernel-density estimation [34–36]. It produces the desired smooth distribution, $Q(\varphi, \sigma)$, by convolving a kernel function with the sampled phase positions $\{\varphi_n\}$,

$$Q(\varphi; \sigma) = \frac{1}{N} \sum_{n=1}^N G(\varphi - \varphi_n; \sigma), \quad (\text{A4})$$

The kernel function, $G(\varphi; \sigma)$, is parametrized by some nonzero smoothing window, or bandwidth, σ . Here, we choose the wrapped-Gaussian function,

$$G(\varphi; \sigma) = \sum_{j=-\infty}^{\infty} \frac{1}{\sqrt{2\pi\sigma^2}} \exp\left[-\frac{(\varphi - j)^2}{2\sigma^2}\right]. \quad (\text{A5})$$

Given the estimated distribution $Q(\varphi, \sigma)$, we may determine its global maximum φ_f according to Sec. IV.

For every k , based on the N samples that each agent has, we compute the distributions $Q_A^{(k)}(\varphi; e^{S_A^{(k)}})$ and $Q_B^{(k)}(\varphi; e^{S_B^{(k)}})$ from Eq. (A4) on lattices of spacings $e^{S_A^{(k)}}/10^3$ and $e^{S_B^{(k)}}/10^3$, respectively. Using Eq. (7), we find $\varphi_{f,A}^{(k)}$ and $\varphi_{f,B}^{(k)}$. There are more involved discretization-free techniques to find extrema of kernel-density estimators [43–45]. Since $\varphi_{f,A}^{(k)}$ and $\varphi_{f,B}^{(k)}$ will only differ by about e^S/\sqrt{N} , with $N = 500$, using a discretization $e^S/10^3$ should not impact the results.

-
- [1] J. C. Dunlap, Molecular bases for circadian clocks, *Cell* **96**, 271 (1999).
- [2] Y. Liao and M. J. Rust, The circadian clock ensures successful DNA replication in cyanobacteria, *Proc. Natl. Acad. Sci. U.S.A.* **118**, e2022516118 (2021).
- [3] G. Banfalvi, *Cell Cycle Synchronization*, 2nd ed., Methods in Molecular Biology (Springer, New York, 2017).
- [4] F. Rieke, D. Warland, R. R. de Ruyter van Steveninck, and W. Bialek, *Spikes: Exploring the neural code* (MIT Press, 1997).
- [5] Z. F. Mainen and T. J. Sejnowski, Reliability of spike timing in neocortical neurons, *Science* **268**, 1503 (1995).
- [6] R. R. de Ruyter van Steveninck, G. D. Lewen, S. P. Strong, R. Koberle, and W. Bialek, Reproducibility and variability in neural spike trains, *Science* **275**, 1805 (1997).
- [7] Y. Penn, M. Segal, and E. Moses, Network synchronization in hippocampal neurons, *Proc. Natl. Acad. Sci. USA* **113**, 3341 (2016).
- [8] S. Trolier-McKinstry, S. Zhang, A. J. Bell, and X. Tan, High-performance piezoelectric crystals, ceramics, and films, *Annu. Rev. Mater. Res.* **48**, 191 (2018).
- [9] S. Strogatz, *Synch: The emerging science of spontaneous order* (Penguin UK, 2004).
- [10] A. Pikovsky, M. Rosenblum, and J. Kurths, *Synchronization: a universal concept in nonlinear sciences*, Vol. 12 (Cambridge University Press, 2003).
- [11] D. J. T. Sumpter, The principles of collective animal behaviour, *Philos. Trans. R. Soc. B* **361**, 5 (2006).
- [12] A. Arenas, A. Díaz-Guilera, J. Kurths, Y. Moreno, and C. Zhou, Synchronization in complex networks, *Phys. Rep.* **469**, 93 (2008).
- [13] A. Pikovsky, Synchronization and stochastization of array of

- self-excited oscillators by external noise, *Radiophys. Quantum Electron* **27**, 390 (1984).
- [14] A. S. Pikovsky and J. Kurths, Coherence resonance in a noise-driven excitable system, *Phys. Rev. Lett.* **78**, 775 (1997).
- [15] J. Teramae and D. Tanaka, Robustness of the noise-induced phase synchronization in a general class of limit cycle oscillators, *Phys. Rev. Lett.* **93**, 204103 (2004).
- [16] D. S. Goldobin and A. Pikovsky, Synchronization and desynchronization of self-sustained oscillators by common noise, *Phys. Rev. E* **71**, 045201 (2005).
- [17] H. Nakao, K. Arai, and Y. Kawamura, Noise-induced synchronization and clustering in ensembles of uncoupled limit-cycle oscillators, *Phys. Rev. Lett.* **98**, 184101 (2007).
- [18] K. Nagai and H. Nakao, Experimental synchronization of circuit oscillations induced by common telegraph noise, *Phys. Rev. E* **79**, 036205 (2009).
- [19] H. Nakao, K. Arai, K. Nagai, Y. Tsubo, and Y. Kuramoto, Synchrony of limit-cycle oscillators induced by random external impulses, *Phys. Rev. E* **72**, 026220 (2005).
- [20] J. A. Eaton, B. Moths, and T. A. Witten, Criterion for noise-induced synchronization: Application to colloidal alignment, *Phys. Rev. E* **94**, 032207 (2016).
- [21] Y. Song and T. A. Witten, Stochastic synchronization induced by noise, *Phys. Rev. E* **106**, 044207 (2022).
- [22] T. Yamamoto, I. Oowada, H. Yip, A. Uchida, S. Yoshimori, K. Yoshimura, J. Muramatsu, S. Goto, and P. Davis, Common-chaotic-signal induced synchronization in semiconductor lasers, *Opt. Express* **15**, 3974 (2007).
- [23] T. Zhou, L. Chen, and K. Aihara, Molecular communication through stochastic synchronization induced by extracellular fluctuations, *Phys. Rev. Lett.* **95**, 178103 (2005).
- [24] V. I. Arnold, *Mathematical Methods of Classical Mechanics*, Graduate Texts in Mathematics (Springer, New York, 1978).
- [25] J. T. Stuart, On the non-linear mechanics of wave disturbances in stable and unstable parallel flows part 1. the basic behaviour in plane poiseuille flow, *J. Fluid Mech.* **9**, 353 (1960).
- [26] J. Watson, On the non-linear mechanics of wave disturbances in stable and unstable parallel flows part 2. the development of a solution for plane poiseuille flow and for plane couette flow, *J. Fluid Mech.* **9**, 371 (1960).
- [27] S. B. S. Khalsa, M. E. Jewett, C. Cajochen, and C. A. Czeisler, A phase response curve to single bright light pulses in human subjects, *J. Physiol.* **549**, 945 (2003).
- [28] N. W. Schultheiss, A. A. Prinz, and R. J. Butera, eds., *Phase Response Curves in Neuroscience*, Springer Series in Computational Neuroscience (Springer, New York, 2012).
- [29] S. Hata, T. Shimokawa, K. Arai, and H. Nakao, Synchronization of uncoupled oscillators by common gamma impulses: From phase locking to noise-induced synchronization, *Phys. Rev. E* **82**, 036206 (2010).
- [30] T. M. Cover and J. A. Thomas, *Elements of information theory*, 2nd ed. (Wiley-Interscience, 2006).
- [31] J. D. Victor, Binless strategies for estimation of information from neural data, *Phys. Rev. E* **66**, 051903 (2002).
- [32] Q. Wang, S. R. Kulkarni, and S. Verdu, Divergence estimation for multidimensional densities via k -nearest-neighbor distances, *IEEE Trans. Inf. Theory* **55**, 2392 (2009).
- [33] J. R. Dorfman, *An Introduction to Chaos in Nonequilibrium Statistical Mechanics* (Cambridge University Press, 1999).
- [34] B. W. Silverman, *Density Estimation for Statistics and Data Analysis* (Chapman & Hall, 1986).
- [35] B. U. Park and J. S. Marron, Comparison of data-driven bandwidth selectors, *J. Am. Statist. Ass.* **85**, 66 (1990).
- [36] S. J. Sheather and M. C. Jones, A reliable data-based bandwidth selection method for kernel-density estimation, *J. R. Statist. Soc. B* **53**, 683 (1991).
- [37] B. W. Silverman, Using kernel-density estimates to investigate multimodality, *J. R. Statist. Soc. B* **43**, 97 (1981).
- [38] E. Mammen, J. S. Marron, and N. I. Fisher, Some asymptotics for multimodality tests based on kernel-density estimates, *Probab. Theory Relat. Fields* **91**, 115 (1992).
- [39] P. Vincent and Y. Bengio, Manifold parzen windows, in *Advances in Neural Information Processing Systems*, Vol. 15, edited by S. Becker, S. Thrun, and K. Obermayer (MIT Press, 2002) p. 825.
- [40] A. Mészáros, J. F. Schumann, J. Alonso-Mora, A. Zgonnikov, and J. Kober, *Robust multi-modal density estimation* (2024), arXiv:2401.10566.
- [41] A. Marsiglietti and V. Kostina, A lower bound on the differential entropy of log-concave random vectors with applications, *Entropy* **20**, 185 (2018).
- [42] J. C. Pang, L. L. Gollo, and J. A. Roberts, Stochastic synchronization of dynamics on the human connectome, *NeuroImage* **229**, 117738 (2021).
- [43] K. Fukunaga and L. Hostetler, The estimation of the gradient of a density function, with applications in pattern recognition, *IEEE Trans. Inf. Theory* **21**, 32 (1975).
- [44] Y. Cheng, Mean shift, mode seeking, and clustering, *IEEE Trans. Pattern Anal. Mach. Intell.* **17**, 790 (1995).
- [45] D. Comaniciu and P. Meer, Mean shift: a robust approach toward feature space analysis, *IEEE Trans. Pattern Anal. Mach. Intell.* **24**, 603 (2002).

SUPPLEMENTARY MATERIAL: EFFECTIVE SYNCHRONIZATION AMID NOISE-INDUCED CHAOS

Appendix S1: Instantaneous fiducial phase

Figure S1 illustrates a phase probability distribution defined in Sec. II of the main text. It pictures a time interval long after the most recent kick, but before the next kick. It shows how the phase distribution $q(\varphi)$ and the fiducial phase φ_f move in time.

Appendix S2: Example of a phase map

In Sec. II of the main text, we defined a ‘‘phase map’’ $\psi(\varphi)$ which encapsulates the effect of a kick on a particular nonlinear oscillator. Here, we illustrate how this phase map is determined for a specific dynamical system and type of kick.

In this example, we construct the phase map for perturbations around the limit cycle of a double-well Stuart-Landau dynamics [25, 26] in the complex plane z . Here, $z \equiv x + iy$ evolves according to

$$\frac{dz}{dt} = \frac{1}{2} [f(z + 0.4 + 0.4i, 5, 2.75) + f(z - 0.4 - 0.4i, -1, -4)], \quad (\text{S1a})$$

where

$$f(z, a, b) = (1 + ai)z - (1 + bi)|z|^2z. \quad (\text{S1b})$$

The numbers were chosen such that a stable periodic orbit would be observed; see full black oval in Fig. S2. The period is $T \simeq 1.98$. We designate some point along the limit-cycle orbit as the phase origin, shown as an open square in Fig. S2. We define the phase position φ of given point on the orbit as the time required to move from the phase origin to the given point, relative to the period T (the black ticks along the black oval in Fig. S2). Thus, at the phase position $\varphi = 1$, the given point has traversed the whole cycle and returned to the phase origin.

We now consider the effect of two particular kicks, defined to be a displacement of z by an amount $0.15 + 0i$ in Fig. S2(a) and $0.45 + 0i$ in Fig. S2(b). We have chosen this displacement so that any point φ on the limit cycle returns to it virtually completely in a time $9T$ or less. Thus after any number of cycles greater than 9, the final phase ψ of the oscillator is constant. Displacements bigger than $\simeq 0.46$ cause some of the initial phases to escape the periodic orbit’s basin of attraction. In that sense, the latter displacement (b) is a very strong forcing; the former (a) is much milder.

If one kicks an oscillator that was at $\varphi = 0$ (empty squares), it will then undergo the trajectories shown with the dashed red curves in Fig. S2. After $9T, 10T, 11T, \dots$, we find, to good accuracy, that it reaches the points marked by solid squares, which is found to have a phase $\psi \simeq -0.13$ for the weak forcing (a) and $\psi \simeq -0.44$ for the strong forcing (b). (As before, ψ is still defined mod 1. However, so to obtain the smooth collection of blue empty points in Fig. S3, we determined integer offsets by counting the number of cycles completed during $9T$ relative to the 9 cycles that an unperturbed oscillator would have completed during $9T$.) Likewise, kicking oscillators that are at $\varphi \simeq 0.35$ (empty triangles) and $\varphi \simeq 0.6$ (empty diamonds), through the dotted-orange and full-blue trajectories, they will, respectively, reach $\psi \simeq 0.73$ and $\psi \simeq 0.36$ for the weak forcing (a) and $\psi \simeq 1.37$ and $\psi \simeq -0.66$ for the strong forcing (b), which are depicted with solid triangles and diamonds. We remind that were the three not kicked, after $9T$ they would have returned back to their original positions (0, 0.35, and 0.6), and that any phases that differ by an integer necessarily correspond to the same point on the orbit.

To determine the final phase ψ for arbitrary initial phases φ , we repeat this process for many closely spaced initial φ ’s. The result is the phase maps shown in Fig. S3, which depend on the displacement (forcing magnitude), shown in Fig. S3. The lags between the initial and final phases are shown with the empty blue symbols in Fig. S2. The squares, triangles, and diamonds correspond to the final phase ψ of $\varphi = 0$, $\varphi \simeq 0.35$, and $\varphi \simeq 0.6$, respectively, under each forcing. Constructing the phase map $\psi(\varphi)$ amounts to taking mod 1 of the resulting lags. Since the system is rotation invariant (as the next kick is also randomly timed according to a uniform distribution $[0, 1)$), we shift all phases such that, arbitrarily, $\psi(\varphi = 0) = 0$. This allows the comparison with the cubic phase map considered in the main text. Upon this shift and taking the moduli, we find the phase maps depicted with connected red points. Indeed the very strong forcing $z \rightarrow z + 0.45$ leads to a very violent phase map (even having an apparent discontinuity in the spreading factor $d\psi/d\varphi$ at $\varphi \simeq 0.32$). The mild forcing $z \rightarrow z + 0.15$, which is the limit with which we are concerned in this work, has given rise to a well-behaved and smooth phase map with a single minimum and maximum. As we explained in the main text, broad minima and maxima are the ones facilitating the formation of sharply-peaked and thence low-entropy distributions. This suggests that the findings of the main text for the simplistic cubic phase map we chose should apply in ‘real-world’ forcings as well.

Appendix S3: Phase map iteration

In Fig. S4 we illustrate the changes in a set of initial phases $\{\varphi_n\}$ through an iteration of the phase map of Eq. (2) of the main text.

Appendix S4: Dependence on stochastic realization

In Fig. 2 of the main text, we show a sequence of distributions obtained for two agents under the influence of common noise. Despite the different initial conditions, for $\Lambda < 0$ we observe synchronization, whereas for $\Lambda > 0$ we observe convergence of ensembles. To emphasize that a common noise is a necessary condition, in Fig. S5 we show two ensembles, starting from the same distribution, which are subjected to different noises. Evidently, since the information about the ambient noise is not shared, the distributions do not synchronize with $\Lambda < 0$ and do not converge for $\Lambda > 0$.

Appendix S5: Synchronization for $\Lambda < 0$

Here we revisit the discussion of Sec. III of the main text for a synchronizing phase map with $\Lambda < 0$. That is, the agents' phases agree up to a gradually-diminishing uncertainty. For $\Lambda < 0$, both distributions $q_A^{(k)}(\varphi)$ and $q_B^{(k)}(\varphi)$ are expected to become a sharp peak centered around the same phase value. To test this, we initiate both distributions to be concentrated uniformly into eccentric narrow sectors of angular width $u = 0.05$, one centered at $\varphi = 0.025$ and the other at $\varphi = 0.525$. While indeed both entropies decay to $-\infty$ (see Fig. S6(b)), both KLDs have reached a *different nonzero* plateau (see Fig. S6(a)).

We can analyze this observation quantitatively. Since each $q_A^{(k)}(\varphi)$ and $q_B^{(k)}(\varphi)$ is very narrow, for a given $\beta^{(k)}$, at most a single $\hat{\varphi}$ contributes appreciably to a given φ during a kick event. Namely, if there is a $\hat{\varphi}$ such that $\psi(\hat{\varphi} + \beta^{(k)}) = \varphi$ and $q_A^{(k)}(\hat{\varphi})$ is within its peak region, then it is given by

$$q_A^{(k)}(\varphi) \simeq q_A^{(k-1)}(\hat{\varphi}) \left| \frac{d\psi}{d\varphi} \Big|_{\hat{\varphi} + \beta^{(k)}} \right|^{-1}, \quad (\text{S3})$$

and the same for a narrow $q_B^{(k)}$. Otherwise, the contribution from other φ 's is negligible. Thus, stochastic-timed forcings may only “stretch” or “contract” narrow unimodal distributions to the same extent. Since both $q_A^{(k)}(\varphi)$ and $q_B^{(k)}(\varphi)$ are centered around the same phase value, the same $\hat{\varphi}$ corresponds to each φ in both distributions. Hence, upon a change of variables $d\varphi = (d\psi/d\varphi)|_{\hat{\varphi} + \beta^{(k)}} d\hat{\varphi}$, we find the KLD by definition

$$D^{(k)}(A\|B) = \int_0^1 d\hat{\varphi} q_A^{(k-1)}(\hat{\varphi}) \ln \frac{q_A^{(k-1)}(\hat{\varphi})}{q_B^{(k-1)}(\hat{\varphi})} = D^{(k-1)}(A\|B), \quad (\text{S4})$$

and similarly $D^{(k)}(B\|A) = D^{(k-1)}(B\|A)$. Thus, indeed the KLD is capable of remaining constant for two infinitely narrow distributions, as they either “stretch” or “contract” *together* to the same extent. Similar reasoning explains why, while the entropies decay to $-\infty$, the difference among them for these two narrow distributions remains constant for low entropy values in Fig. S6(b).

Thus, for $\Lambda < 0$, it is possible to interpret the asymptotically-nonzero KLDs to mean that agent B's “guess” ($q_B^{(k)}(\varphi)$) is not in perfect agreement with agent A's actual distribution ($q_A^{(k)}(\varphi)$). This is misleading in our context, as efficient communication may still be established in the $\Lambda < 0$ scenario. To the contrary, the distributions $q_A^{(k)}(\varphi)$ and $q_B^{(k)}(\varphi)$ described here permit φ_f to be transmitted to arbitrary precision. This nonzero divergence simply stems from $q_A^{(k)}(\varphi)$ and $q_B^{(k)}(\varphi)$ not necessarily attaining the same (almost-zero) width.

From similar considerations, observe the $25 \lesssim k \lesssim 65$ regime in Fig. 3(a) of the main text, where the dynamics of $\Lambda > 0$ is shown. As seen in Fig. 2, $\Lambda = 0.141$ panels of the main text, indeed the distributions are very narrow during these steps (which also manifests in a low entropy in Fig. 3(b) of the main text). This regime mimics the $\Lambda < 0$ case at late times, where the narrow distributions change width together and barely mix, which manifests in a constant KLD in Fig. 3(a) of the main text. As we argued here, this nonzero KLD need not imply that these sharp distributions are not useful for communication, so long as they share means. However, since $\Lambda > 0$, the distributions are bound to get sufficiently wide eventually, continue the mixing, and thus the KLD resumes its decay.

Appendix S6: Effect of the bandwidth

In Sec. IV of the main text, we describe the estimation of a smooth probability function $Q(\varphi, \sigma)$ from a set of samples $\{\varphi_n\}$. In Fig. S7 we show the effect of a different bandwidth σ using sampled $\{\varphi_n\}$'s from the main text.

Appendix S7: fiducial phase differences between agents

In Sec. IV of the main text, we compared the fiducial phases obtained by two independent agents. Their oscillators were subjected to the same phase map $\psi(\varphi)$ and the same kick timings $\{\beta^{(k)}\}$. Since each agent used a finite set of $N = 500$ samples to obtain their $\varphi_f^{(k)}$ after the k 'th kick, their fiducial phases may not fully coincide when they sample an identical distribution. Thus, the agents obtain different values for $\varphi_f^{(k)}$. Figure S8 shows the obtained differences $|\Delta\varphi_f|$ as a scatter plot against the common distribution's entropy, using two different bandwidths, (a) $\sigma = e^S$ and (b) $\sigma = e^S/N$. We interpret these results in the next section.

Appendix S8: Rare misidentifications of fiducial phase

We point out that out of 10^4 data-points for $|\Delta\varphi_f|$ used in Sec. IV of the main text, 88 points lie above the $|\Delta\varphi_f| = e^S$ line (0.9%), typically even a few orders of magnitude above it for high-entropy distributions; see Fig. S8(a). On examination, these points either corresponded to distributions with entropy $S \sim 0$ or proved to be misidentifications, in which the $Q(\varphi; e^S)$'s had two peaks of nearly equal height and the agents made opposite determinations of the global maximum, as a result of the finite samples used to estimate $Q(\varphi; e^S)$. Among these occurrences is the distribution of Fig. S7, where each agent chose a different peak out of the two at 0.41 and 0.93.

Based on this finding, we suggest that the effect of these large $\Delta\varphi_f$'s can be much reduced. Each agent is able to determine the uncertainty of its highest and second highest peak. If the two heights are statistically indistinguishable, the agent cannot obtain an unambiguous φ_f and would not be able infer the other agent's effective phase at that kick. Had this been done in our analysis, the large $|\Delta\varphi_f|$'s could have been reduced for distributions whose entropies are not approaching 0. We anticipate that any remaining large φ_f 's could be made insignificant.

These misidentifications were an important factor in our choice of smoothing width $\sigma = e^S$. Indeed, when we used $\sigma = e^S/N$ (rather than $\sigma = e^S$ of the main text) as a bandwidth, there were 791 misidentified points (8%), which have occurred with distributions of entropies as low as $S = -14$; see Fig. S8(b). In fact, the large concentration of points surrounding $|\Delta\varphi_f| = e^S$ suggests that the bandwidth is too small, and not enough samples are involved in estimating the peak center, raising the error from $|\Delta\varphi_f| \sim e^S/\sqrt{N}$ to just the overall "width" of a given distribution $|\Delta\varphi_f| \sim e^S$. At the same time, in the cases where the identification of the peak was precise (that is, the highest peak clearly dominates over the rest and encapsulated $\sim N$ samples), this smaller bandwidth allowed for an appropriately smaller discrepancy, $|\Delta\varphi_f| \sim (e^S/N)/\sqrt{N}$. Thus, as we expected, smaller bandwidths facilitate smaller deviations, which comes at a cost of more frequent, finite-sample-size-related misidentifications of the highest peak.

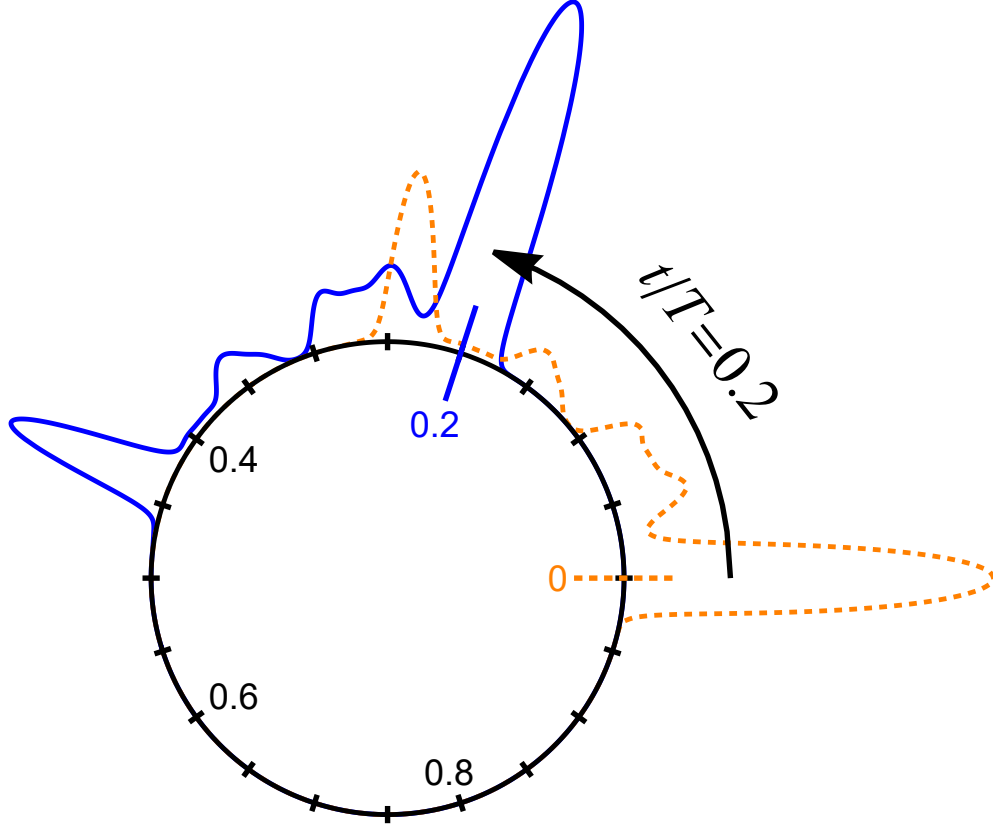


FIG. S1. Relation between the fiducial phase position φ_f and the instantaneous fiducial phase $\varphi_f + 0.2T$ at a later time $t = 0.2T$, as measured by a given agent. Orange dotted curve represents the distribution $q(\varphi)$ for some particular noise history. The highest peak of this distribution is then φ_f , and is marked with a dashed line. At time $t = 0$ this is the actual phase distribution. At a time $t = 0.2T$ later, every phase point, including the agent's own oscillator's phase, has advanced through 0.2 cycles. The probability distribution $q(\varphi - 0.2T)$ and fiducial phase $\varphi_f + 0.2T$ at that moment is shown by the blue line.

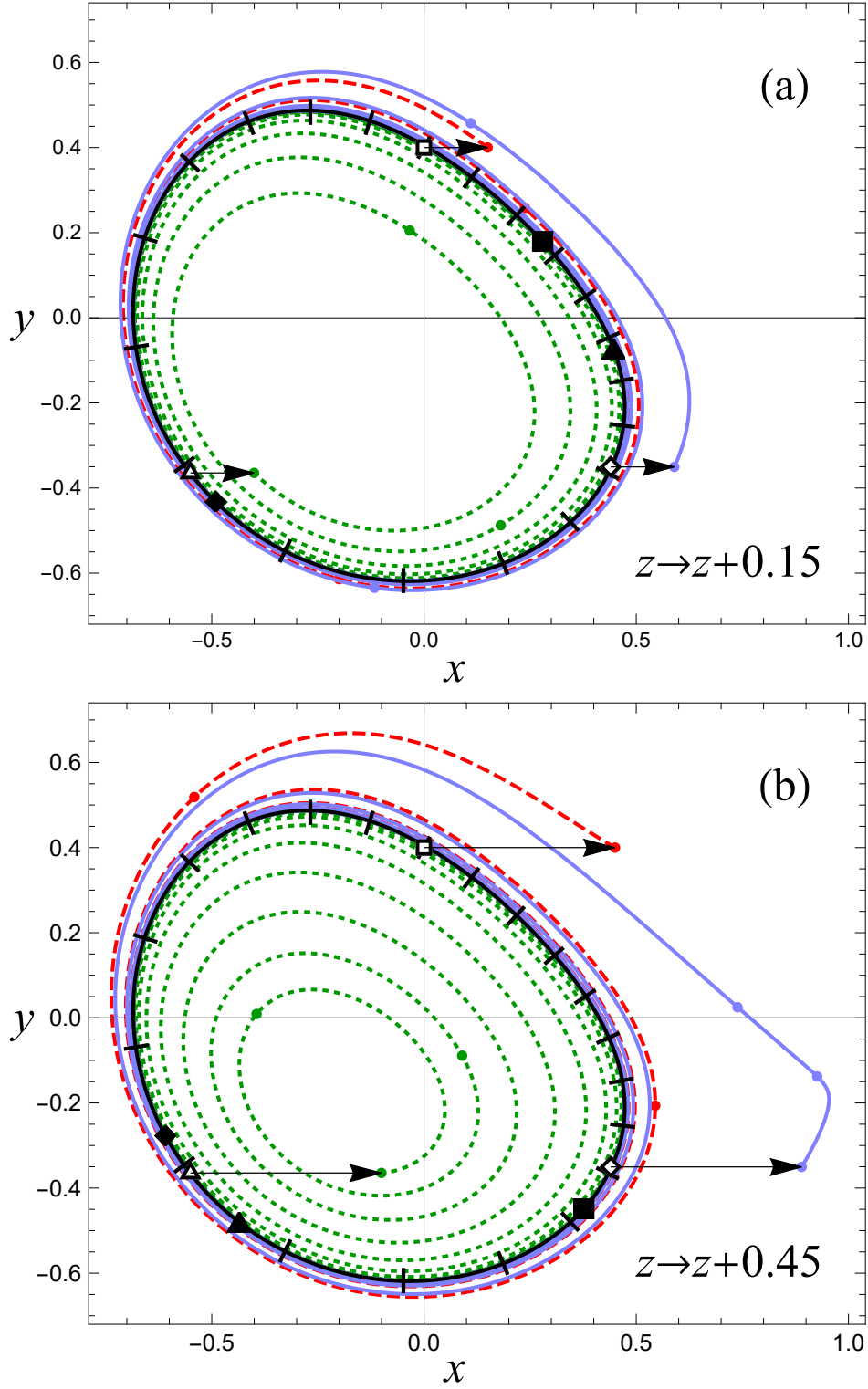


FIG. S2. Trajectories from the dynamical system of Eq. (S1). The limit cycle (period $T = 1.98$) is shown in full black oval. The black ticks along it are equispaced $\varphi \in [0, 1)$ values, separated by $\Delta t/T = 0.05$. ($\varphi = 0$ is located at $0 + 0.4i$, overlapping with the empty square.) We show the resulting trajectories from kicking oscillators positioned at $\varphi = 0$ (empty square), $\varphi \simeq 0.35$ (empty triangle), and $\varphi \simeq 0.6$ (empty diamond) by (a) $z \rightarrow z + 0.15$ and (b) $z \rightarrow z + 0.45$. The first three small points on each trajectory are the positions of the oscillators after $t = 0, (1/2)T, T$. After a time $9T$, the oscillators reach the stable orbit with new phase values, $\psi \simeq -0.13$ (full square), $\psi \simeq 0.73$ (full triangle), and $\varphi \simeq 0.36$ (full diamond) in (a), and $\psi \simeq -0.44$ (full square), $\psi \simeq 1.37$ (full triangle), and $\varphi \simeq -0.66$ (full diamond) in (b).

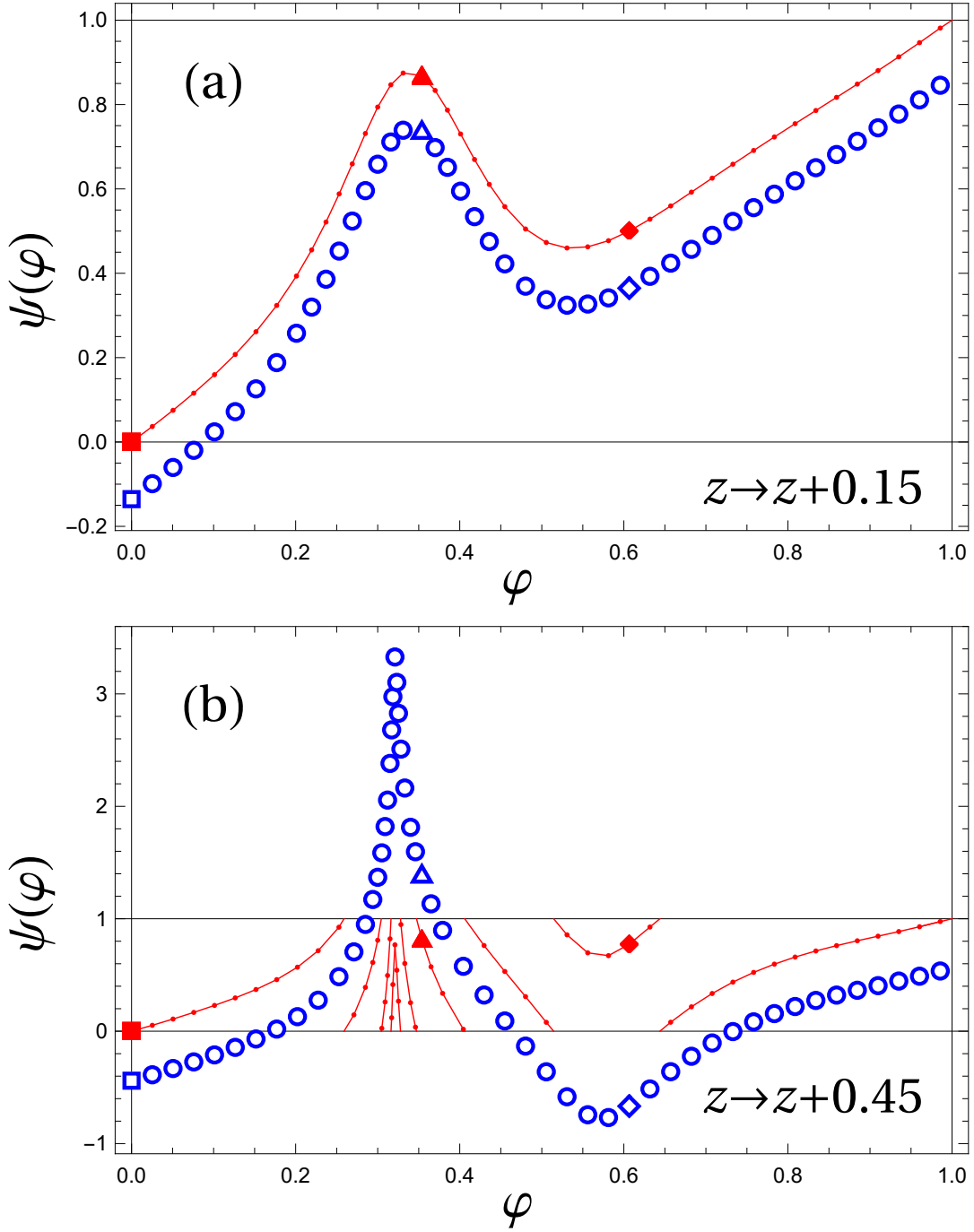


FIG. S3. Phase lags from the dynamical system of Eq. (S1). Empty blue symbols are phase shifts as seen in Fig. S2. The square, diamond, and triangle symbols correspond to the three trajectories in Fig. S2. Since only the fractional parts of phases are significant, each symbol was shifted upwards or downwards by an integer so as to obtain a continuous dependence in φ . In addition, this curve would be shifted vertically and horizontally by choosing a different point on the orbit as the phase origin. Red points show the standardized phase map as used in the main text. Namely, the phase origin and integer-valued shifting were chosen so that $\psi(0) = 0$. Further, each $\psi(\varphi)$ value was shifted to lie between 0 and 1.

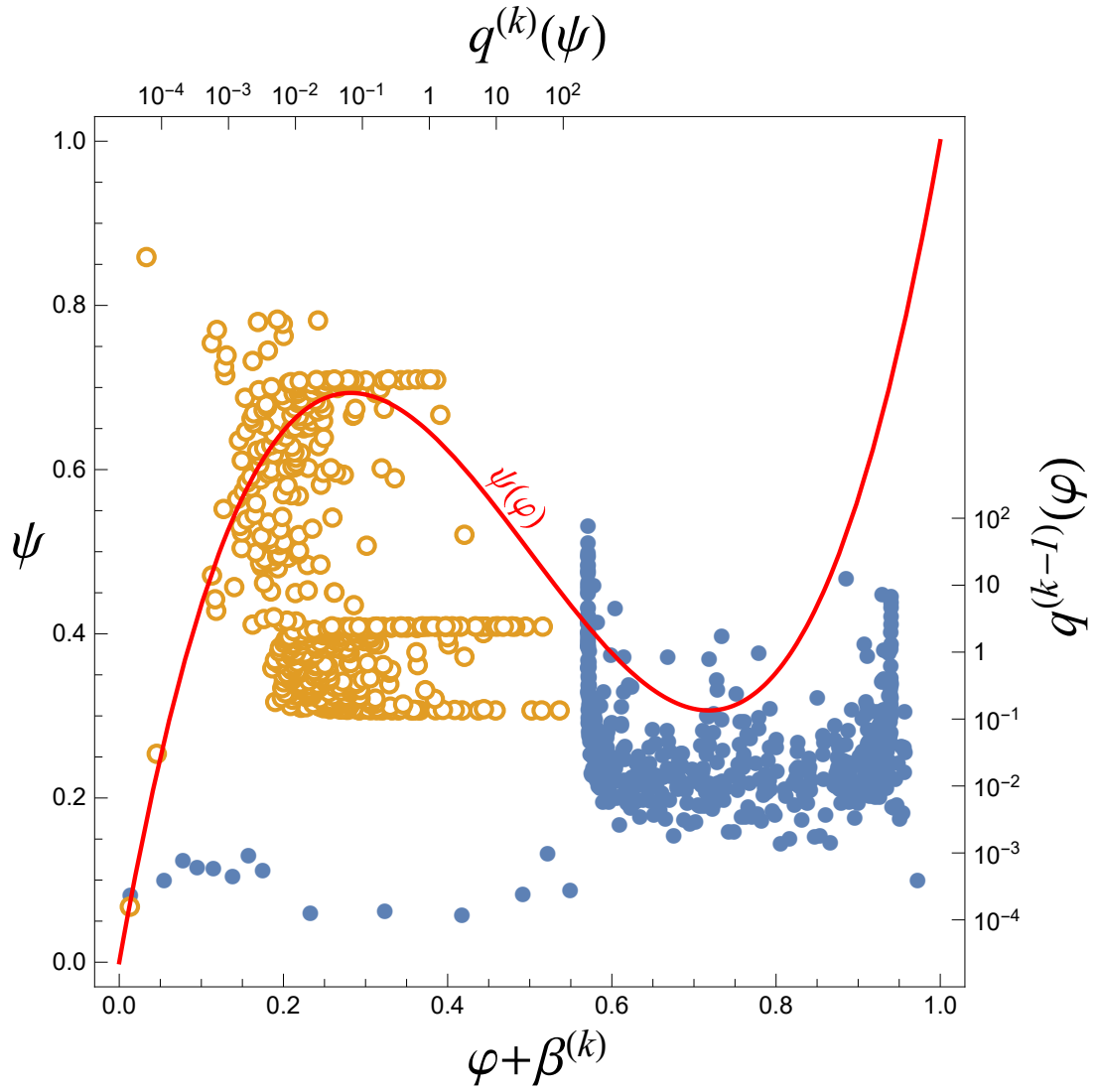


FIG. S4. Two phase distributions $q^{(k)}(\varphi)$ before (blue full circles) and after (orange empty circles, with inflected axes) a kick, obtained for a typical realization of the cubic phase map (Eqs. (1) and (2) of the main text) with $A = 9.32$ ($\Lambda = 0.141$). The cubic phase map is drawn with a red line. One sees how the ‘sporadic’ region of the initial distribution in the vicinity the phase map’s extremum ($\varphi \simeq 0.7$) is condensed into a prominent peak at $\psi \simeq 0.3$. Conversely, the surroundings of the peak at $\varphi \simeq 0.95$ are widened at $\psi = 0.7$, while its height decreased from $\mathcal{O}(10)$ to $\mathcal{O}(1)$. The phase distributions are sampled from $N = 500$ oscillators.

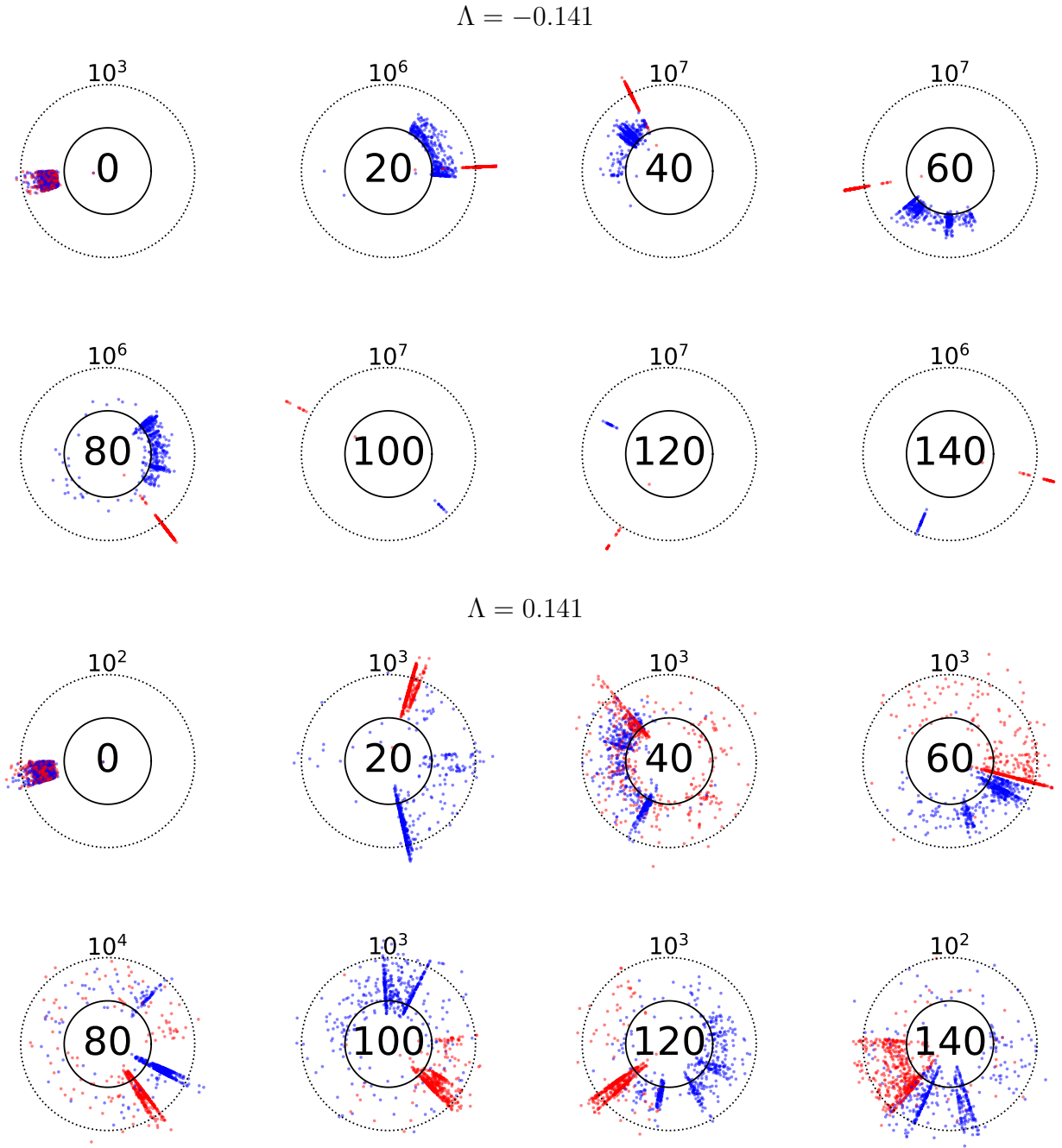


FIG. S5. A sequence of two, initially-identical phase distributions $q_A^{(k)}(\varphi)$ (red) and $q_B^{(k)}(\varphi)$ (blue) subjected to different noises in a typical realization of Eq. (1) and Eq. (2) of the main text with either $\Lambda = -0.141$ ($A = 7.32$) or $\Lambda = 0.141$ ($A = 9.32$), as indicated. The initial distributions are uniform, $\varphi \sim U[0.5, 0.55]$. The distributions are drawn on a circle so the periodicity mod 1 of the phase circle is apparent. The radial axis shows the distributions' values $q(\varphi)$ on a log scale, where $q(\varphi) = 1$ for the inner full circle and as indicated for the outer dotted circles. The kick numbers k are shown inside the inner circle. Since the noise is different for each ensemble, $\Lambda < 0$ produces different synchronized states, whereas $\Lambda > 0$ produces erratic distributions that do not converge unto each other. The distributions are sampled using $N = 500$ oscillators via the nearest-neighbor distances; see Eq. (A1) of the main text. The initial samples drawn for ensemble A are copied to ensemble B, so the starting point is truly identical.

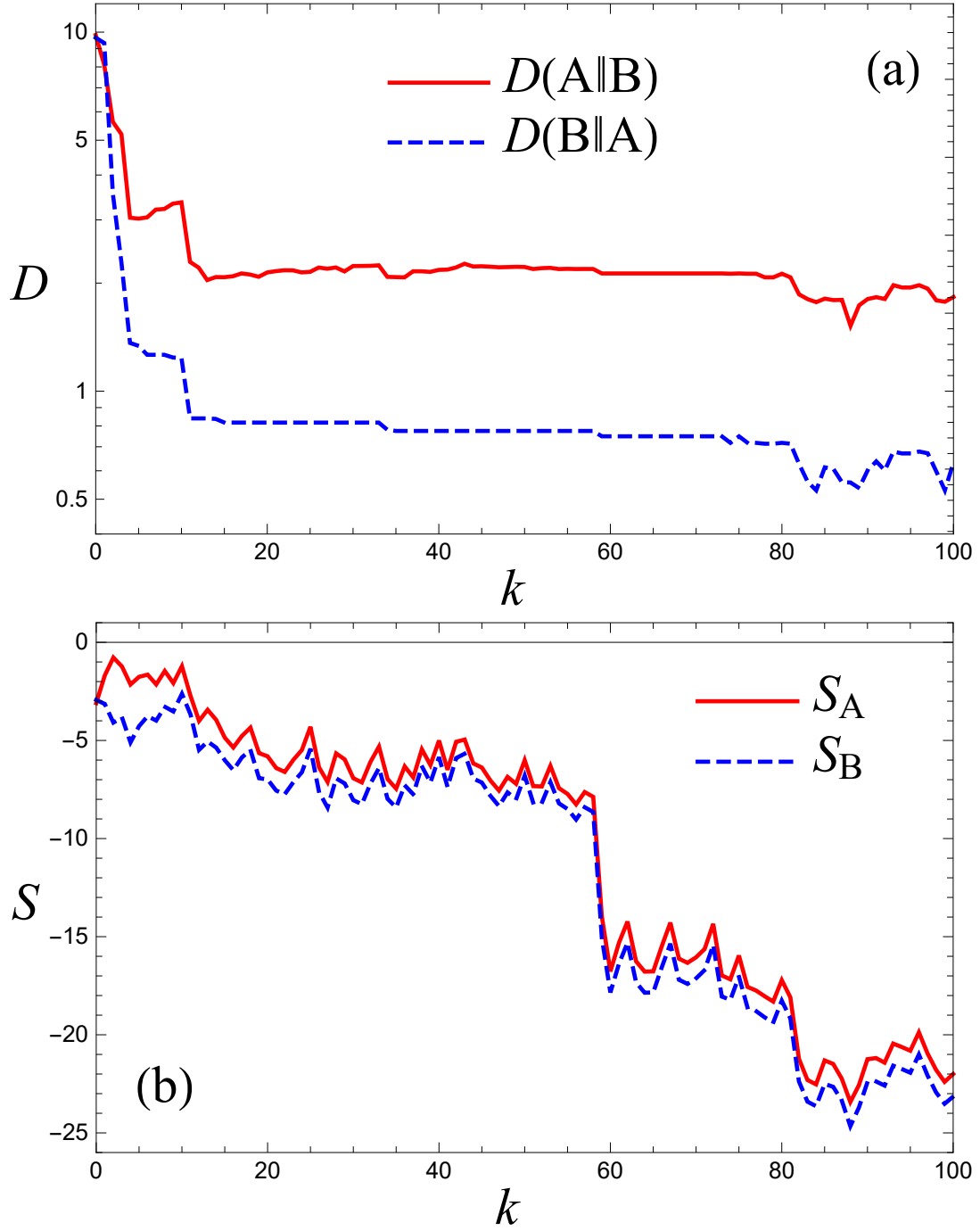


FIG. S6. (a) Kullback-Leibler divergences (KLDs) $D(A||B)$ and $D(B||A)$ among two distributions and (b) entropies S_A and S_B of each distribution, as obtained for the waiting time realization $\{\beta^k\}$ of Fig. 2 of the main text with $\Lambda = -0.141$. The number of phase samples is $N = 500$. The initial distribution per ensemble is obtained with width $u = 0.05$. The numerical errors in the estimation of the KLDs and entropies are $\Delta D = 0.05$ and $\Delta S = 0.2$, respectively.

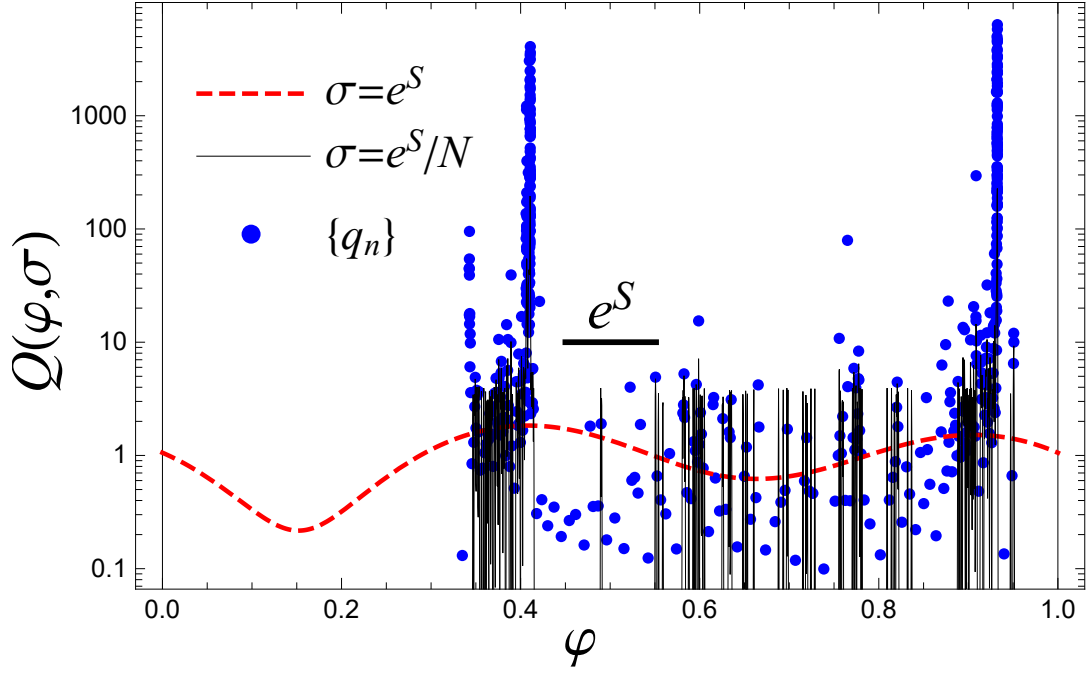


FIG. S7. Illustration of the kernel-density estimation method. Here we estimate the distribution from $N = 500$ phase samples obtained at $k = 100$ by agent B during the realization of Fig. 2 of the main text for $\Lambda = 0.141$. The density estimate of Eq. (A1) of the main text is shown in points. The kernel-density estimate, $Q(\varphi; \sigma)$, is carried out with either $\sigma = e^S$ (the bandwidth we use throughout Sec. IV of the main text; dashed red curve) or $\sigma = e^S/N$ (the alternative extreme; thin solid black curve). $S = -2.29$ for this distribution using Eq. (A2) of the main text. A scale bar of e^S is shown for reference with a thick black horizontal line. Clearly, the result of the latter bandwidth is not statistically significant, as it is comparable to the nearest-sample distances. The analysis in the main text is carried out with the former bandwidth.

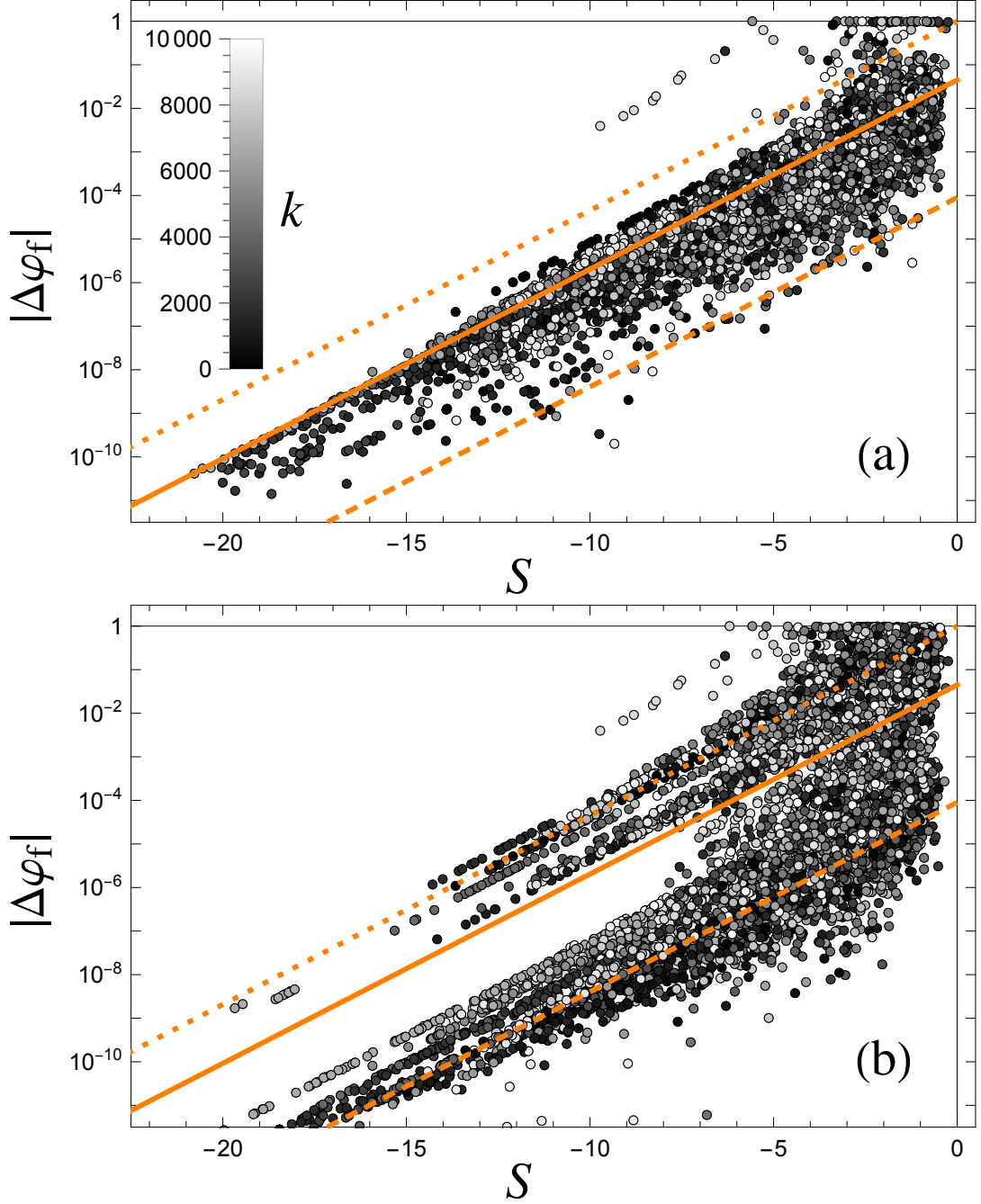


FIG. S8. A scatter plot of deviations in the fiducial phases of each party $\Delta\varphi_f^{(k)} = \varphi_{f,A}^{(k)} - \varphi_{f,B}^{(k)}$ against the entropy of their distributions $S^{(k)} = (S_A^{(k)} + S_B^{(k)})/2$, using bandwidths (a) $\sigma = e^S$ (used for Fig. 5 of the main text) and (b) $\sigma = e^S/N$. Each $(S, |\Delta\varphi_f|)$ point is computed given a pair of distributions $Q_A^{(k)}$ and $Q_B^{(k)}$ obtained after kicks (with $\Lambda = 0.141$) $k = 1, \dots, 10^4$. For completeness, the points' shading encodes the kick at which it was obtained, as indicated. The orange dotted, solid, and dashed lines are, respectively, $|\Delta\varphi_f| = e^S$, $|\Delta\varphi_f| = e^S/\sqrt{N}$, and $|\Delta\varphi_f| = e^S/N^{3/2}$.